3.0 DISTRIBUTED MEASUREMENTS OF AIR QUALITY AND METEOROLOGY

Section 3.1. Spatial, Seasonal, and Inter-annual Aspects of Wintertime Ozone

Seth Lyman, Marc Mansfield, Howard Shorthill, Randy Anderson, Chad Mangum, Jordan Evans, and Tate Shorthill

Office of Commercialization and Regional Development, Utah State University, Vernal, Utah

Section 3.2. Observations and Numerical Modeling of the Atmospheric Boundary Layer in the Uinta Basin

John Horel, Erik Crosman, and Erik Neemann

Department of Atmospheric Sciences, University of Utah, Salt Lake City, Utah

Section 3.3. Use of the CALMET Diagnostic Model to Simulate Winter Inversions

Michael Christiansen and Trevor O'Neil

Department of Chemistry, Utah State University, Vernal, Utah

3.1 Spatial, Seasonal, and Inter-annual Aspects of Wintertime Ozone

3.1.1 Introduction

Ozone concentrations have been measured continuously in the Uinta Basin since fall 2009. During winter 2009-10, monitoring stations at Ouray and Red Wash observed ozone concentrations that exceeded the Environmental Protection Agency (EPA) standard. Following the discovery of this new phenomenon, stakeholder concern led to the establishment of several additional air quality monitoring stations to support subsequent studies. Seventeen stations operated around the Uinta Basin during winter 2010-11, and 30 operated during winter 2011-12. Martin et al. (2011) and Lyman and Shorthill (2013) highlight the results of these studies. This section contains an analysis of ozone, precursor, and meteorology data from 20 monitoring sites that operated around the Basin during winter 2012-13, and an analysis of variability across the four years of available ozone data.

3.1.2 Methods

3.1.2.1 Ozone Measurements

Ten of the air quality monitoring stations in the Uinta Basin during winter 2012-13 were operated by Utah State University (USU), and ten were operated by other organizations. Table 3-1 contains a list of all monitoring stations, including locations, elevations, and responsible operators. Data and methods used for stations operated by other organizations were obtained from EPA's AQS database (https://ofmext.epa.gov/AQDMRS/aqdmrs.html). We utilized 2B Technology Model 205 or 202 ozone monitors at most of the stations, and we operated an Ecotech Model 9810 ozone analyzer at the Horsepool site. We performed calibration checks at all USU stations at least every other week using NIST-traceable ozone standards. Calibration

checks passed if monitors reported in the range of ±5 ppb when exposed to 0 ppb ozone, and if monitors were within ±7% deviation from expected values when exposed to 90 and 140 ppb ozone. We only included data bracketed by successful calibration checks in the final dataset.

Table 3-1. Air quality monitoring stations that operated during winter 2012-13.

Site Name	Operator	Data Availability	Latitude	Longitude	Elevation (m)	VOC	NO_x
Dinosaur NM	NPS	AQS dbase	40.4371	-109.3047	1463	N/A	N/A
Duchesne	USU	USU	40.1615	-110.4011	1682	N/A	N/A
Fruitland	UDAQ	AQS dbase	40.2087	-110.8403	2021	canister	active NO, NO_2
Seven Sisters	USU	USU	39.9813	-109.3454	1618	canister	passive NO_2
Gusher	USU	USU	40.2935	-109.6575	1557	N/A	N/A
Horsepool	USU	USU	40.1437	-109.4672	1569	active	active NO, NO_2, NO_y
Lapoint	USU	USU	40.4040	-109.8157	1674	N/A	N/A
Little Mtn.	USFS	AQS dbase	40.5368	-109.7001	2624	N/A	N/A
Mountain Home	USU	USU	40.4319	-110.3821	2234	N/A	N/A
Myton	EPA/STI	AQS dbase	40.1948	-110.0622	1550	N/A	active NO, NO_2
Ouray	EPA/Golder	AQS dbase	40.0548	-109.6880	1464	N/A	active NO, NO_2
Rabbit Mtn.	Enefit/Tetra.	AQS dbase	39.8687	-109.0973	1879	N/A	active NO, NO_2
Rangely	NPS/BLM	AQS dbase	40.0869	-108.7616	1648	N/A	active NO, NO_2
Red Wash	EPA/Golder	AQS dbase	40.1972	-109.3525	1689	N/A	active NO, NO_2
Roosevelt	UDAQ/USU	AQS dbase	40.2942	-110.0090	1587	active	active NO, NO_2, NO_y
Sand Wash	USU	USU	39.8390	-109.9150	1416	N/A	N/A
Seep Ridge	USU	USU	39.7539	-109.5460	1975	N/A	N/A
Vernal	UDAQ	AQS dbase	40.4531	-109.5097	1606	canister	active NO, NO_2
Wells Draw	USU	USU	40.0670	-110.1510	1768	canister	Passive NO_2
Whiterocks	EPA/STI	AQS dbase	40.4694	-109.9304	1841	N/A	active NO, NO_2

3.1.2.2 Ozone Precursor Measurements

We measured NO, true NO_2 (via a photolytic converter), and NO_y at Roosevelt and Horsepool with AQD/Teledyne-API and Ecotech systems, respectively, and calibrated the systems weekly with NO standards, monthly with NO_2 standards via gas phase titration, and at the beginning and end of the campaign with nitric acid and n-butyl nitrate permeation tubes (for NO_y). A number of sites operated by other organizations measured NO and NO_2 via a molybdenum converter-based system (measurement contains some NO_y), and we obtained these data from EPA's AQS database. We performed supplemental NO_2 measurements at some sites from February 1 through February 8 using Radiello NO_2 passive samplers (Table 3-1). We deployed Radiello samplers for one week and analyzed them according to Radiello protocols on a Dionex ion chromatograph. Radiello samples were blank corrected and also corrected to concentrations of NO_2 measured with automated instruments at co-located sites.

We measured 57 ozone-forming nonmethane hydrocarbons (NMHC) in 30-minute and hourly samples at Horsepool and Roosevelt, respectively, during January and February. NMHC were analyzed by sample concentration on activated carbon traps, followed by desorption into automated gas chromatography-flame ionization detection systems. We calibrated these systems every other week with certified gas standards. We also performed supplemental NMHC measurements at some sites from February 1 through February 8 using evacuated stainless steel canisters. Canisters were filled from 7 to 9 AM on 1, 3, 6, and 8 February. Some of these samples were analyzed with the Roosevelt automated gas chromatograph, but most were analyzed by a commercial laboratory using gas chromatography and flame ionization detection. Canister samples utilized automated sampling timers and critical orifice-based flow controllers. All wetted parts were either stainless steel or stainless steel coated with deactivated fused silica. All canister sampling components were cleaned between each use by repeatedly flushing with hot, humidified nitrogen. EPA PAMS compounds (EPA, 2003) were measured by the automated systems at Horsepool and Roosevelt, and PAMS compounds and methanol were measured with canister systems. Methanol was analyzed via gas chromatography and mass spectrometry by a commercial laboratory.

3.1.2.3 Meteorological Measurements

We operated solar radiation sensors, including incoming and outgoing short wave, long wave, UV-A, and UV-B at Horsepool, and incoming and outgoing shortwave radiation at Roosevelt. We operated a comprehensive, research grade meteorological instrument suite at Horsepool and lower cost meteorological measurements (Davis VantagePro) at some other sites. In addition, we downloaded meteorological data collected by others from the EPA AQS database and from http://mesowest.utah.edu.

3.1.2.4 Spatial Data Analysis

Data from all sites were visualized and interpolated using ArcGIS software. Relationships among measured parameters and a variety of spatial variables were investigated using ArcGIS and SPSS software. The following variables were considered in terms of proximity to study sites (5, 10, 15, 20, 25, or 50 km radius):

- Number of producing wells (oil, gas, both),
- Amount of oil and gas production (February 2013),
- Number of drill rigs,
- Number of compressor stations and gas plants (with estimated NO_x and VOC emissions),
- Number and surface acres of produced water ponds,
- Human population,
- Elevation, and
- Difference between elevation of site and of surrounding terrain.

These parameters were analyzed in correlation and multiple regression analyses to determine the best predictors of observed ozone and precursor concentrations.

3.1.3 Results and Discussion

3.1.3.1 Ozone Concentrations and Distribution

Measurements made in the Uinta Basin show that, relative to the three previous winter seasons, the winter of 2012-13 had the highest number of ozone exceedance days, highest maximum concentrations of ozone, and largest affected area of elevated ozone. Five research sites experienced more than 30 days of exceedances of EPA's National Ambient Air Quality Standard (NAAQS) during the 2012-13 season[1]. The only sites in the Basin that had fourth highest daily maximum 8-hour average ozone concentrations below 75 ppb were those more than 2000 m above sea level (Tables 3-1 and 3-2).

In contrast to conditions within the Basin, air quality monitoring stations outside of the Uinta Basin but within other intermountain West basins, including those within Wyoming's Upper Green River Basin, did not experience elevated ozone during the winter of 2012-13 (Table 3-2). Hall et al. (2013) analyzed the relationship between inversion conditions, snow cover and ozone in several intermountain West basins. While pointing out that further investigation is needed, Hall et al. concluded that basins without intensive oil and gas production do not experience high winter ozone levels even when strong inversions and snow cover are present. One potential explanation for this result is that basins without large amounts of oil and gas production may have lower VOC or NOx concentrations or VOC/NOx ratios that are less conducive to ozone formation. However, further study would be needed to confirm this.

The Uinta Basin experienced seven distinct inversion episodes during which ozone at multiple monitoring stations exceeded the NAAQS (Figure 3-1). Of these, a 13-day episode that began 15 January and continued through 27 January was the longest. Episodes in January and early February tended to be longer, whereas episodes in late February and early March were shorter and exhibited more rapid increases in ozone concentrations. The highest ozone concentrations of the study period were observed in early March, while the greatest number of sites exceeded the NAAQS in late January. Adequate snow cover and a series of prolonged inversion conditions (Figure 3-2) allowed for the observed ozone production. As soon as temperatures warmed enough to melt the snow from the Basin, which occurred around 10 March, significant ozone production ceased.

[1] The NAAQS for ozone is 75 ppb, calculated over three calendar years as the average of the fourth highest 8-hr average daily maximum ozone concentration, though any measured concentration above 75 ppb commonly is referred to as "exceedance."

Table 3-2. Statistics for 8-hour average ozone concentrations at sites around the Uinta Basin and at select sites in Utah and the intermountain West from November 2012 through March 2013.

Sites within Uinta Basin	Mean	Median	Max	Min	4th Highest Daily Max	Days of Exceedance
Dinosaur NM	45.8	41.5	126.0	2.0	113.4	26
Duchesne	34.7	34.1	112.4	2.6	87.1	12
Fruitland	39.8	41.6	64.5	5.8	60.5	0
Gusher	58.9	53.6	129.7	13.7	117.6	38
Horsepool	57.8	49.7	139.0	17.0	131.5	41
Lapoint	65.0	59.9	115.6	30.8	109.4	26
Little Mtn.	49.4	49.7	72.3	29.3	66.9	0
Mountain Home	46.8	46.6	74.7	14.9	71.0	0
Myton	52.6	48.5	109.4	15.6	97.7	17
Ouray	47.7	39.9	141.6	6.1	132.4	39
Rabbit Mtn.	44.6	43.0	107.3	18.1	82.5	8
Rangely	38.2	35.8	106.1	6.1	91.0	11
Red Wash	50.1	42.5	124.0	11.4	114.0	36
Roosevelt	44.9	40.1	110.8	9.8	104.0	29
Sand Wash	55.0	49.5	127.5	11.1	122.0	33
Seep Ridge	48.7	47.3	95.1	14.9	80.8	8
Seven Sisters	47.4	41.1	152.0	4.0	137.7	31
Vernal	37.1	33.4	114.9	5.4	102.1	22
Wells Draw	49.5	45.8	131.5	15.1	108.0	26
Whiterocks	55.9	54.8	95.7	31.8	86.8	7
Sites outside Uinta Basin	**Mean**	**Median**	**Max**	**Min**	**4th Highest Daily Max**	**Days of Exceedance**
Boulder (WY)	31.8	32.4	49.8	5.8	47.6	0
Idaho Falls	35.1	35.7	51.2	9.2	49.0	0
Logan	17.5	16.8	44.0	2.0	43.3	0
Meeker	39.7	40.6	59.1	20.8	55.9	0
Price	34.9	35.3	57.8	8.4	51.1	0
Rifle	22.0	21.5	51.6	2.0	46.6	0
Salt Lake City	15.9	14.0	47.8	2.0	46.0	0

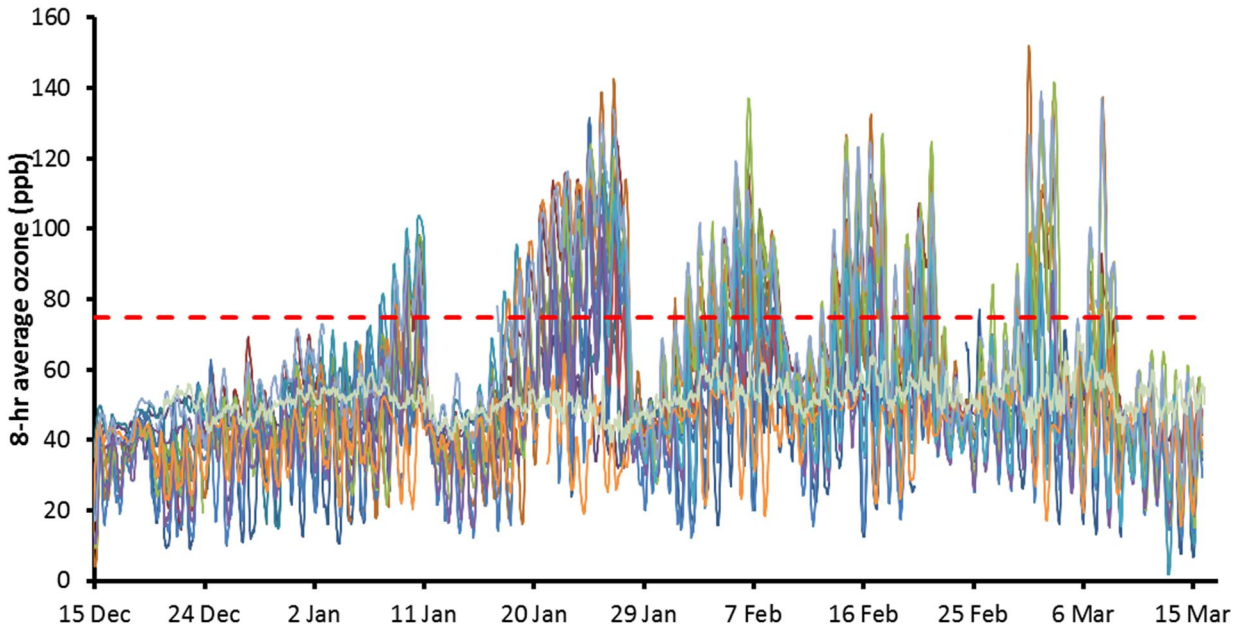

Figure 3-1. Time series of 8-hour average ozone concentrations at all monitoring sites in the Uinta Basin, winter 2012-13. EPA NAAQS of 75 ppb is shown as a red dashed line.

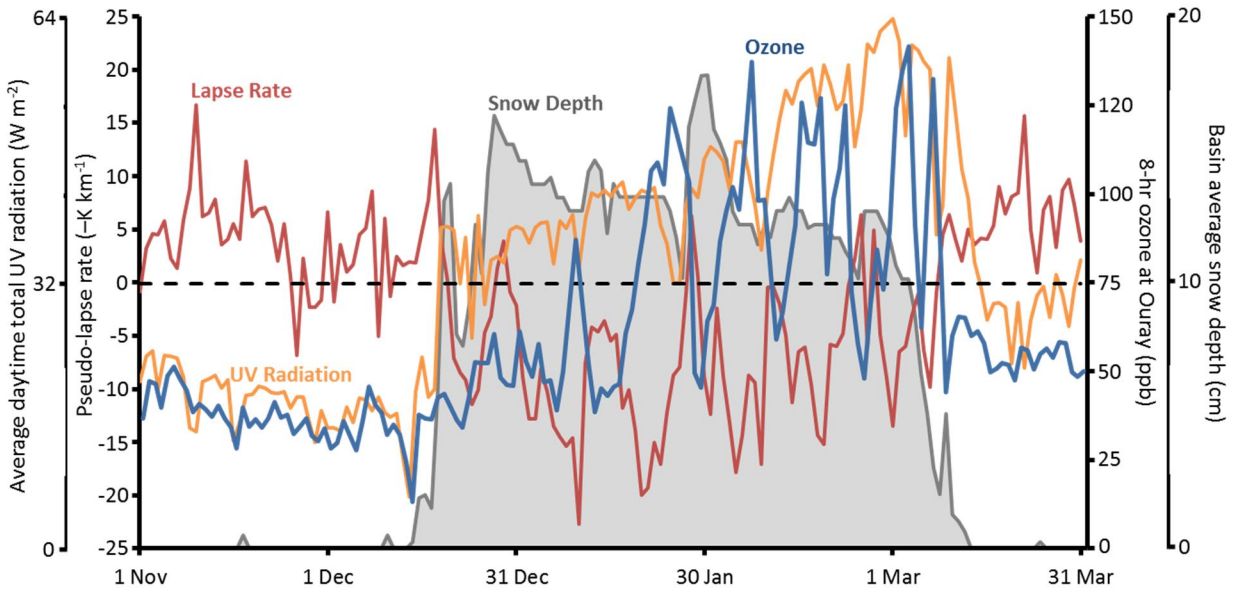

Figure 3-2. Time series of average snow depth from five stations in the Uinta Basin, pseudo-lapse rate for the Basin, 8-hour average ozone at Ouray, and average total daytime UV-A and UV-B radiation (average during daytime hours of the sum of upwelling and downwelling UV-A and UV-B) at Horsepool, winter 2012-13. The pseudo-lapse rate was derived from the change in temperature with elevation at surface meteorological stations in the Basin. The dashed black line indicates a lapse rate of zero and an ozone concentration of 75 ppb. A more negative lapse rate indicates a stronger inversion.

Highest ozone concentrations were observed consistently in the area of the Basin that lies south of Vernal containing a high density of natural gas wells (Figures 3-3, 3-4, and 3-5), though ozone distribution exhibited unique characteristics during different inversion episodes. Figure 3-3 shows that for the entire study period, high elevation sites and sites on the margins of the Basin had the lowest ozone concentrations, while lower elevation sites and sites in the area south of Vernal had the highest.

During the 13-day inversion episode that culminated on 26 January, elevated ozone concentrations extended far beyond the Ouray-Horsepool-Seven Sisters area south of Vernal, and eight-hour average ozone for that day exceeded 100 ppb at ten sites, including sites on the edge of the Basin like Rangely and Rabbit Mountain (Figure 3-4). In contrast, during a shorter inversion episode in early March, only four sites exceeded 100 ppb, and many sites on the margins of the Basin, experienced no exceedances of the NAAQS for ozone (Figure 3-5).

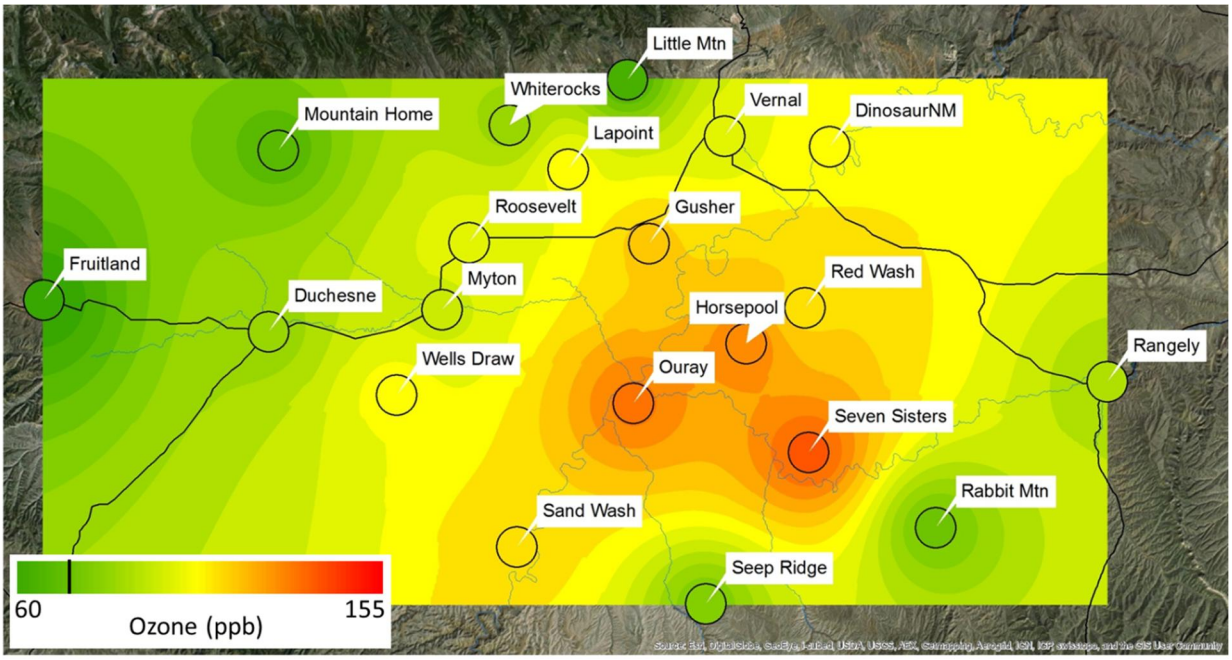

Figure 3-3. Fourth-highest daily maximum 8-hour average ozone concentrations for all sites in the Uinta Basin, winter 2012-13. The black line on the color scale indicates 75 ppb.

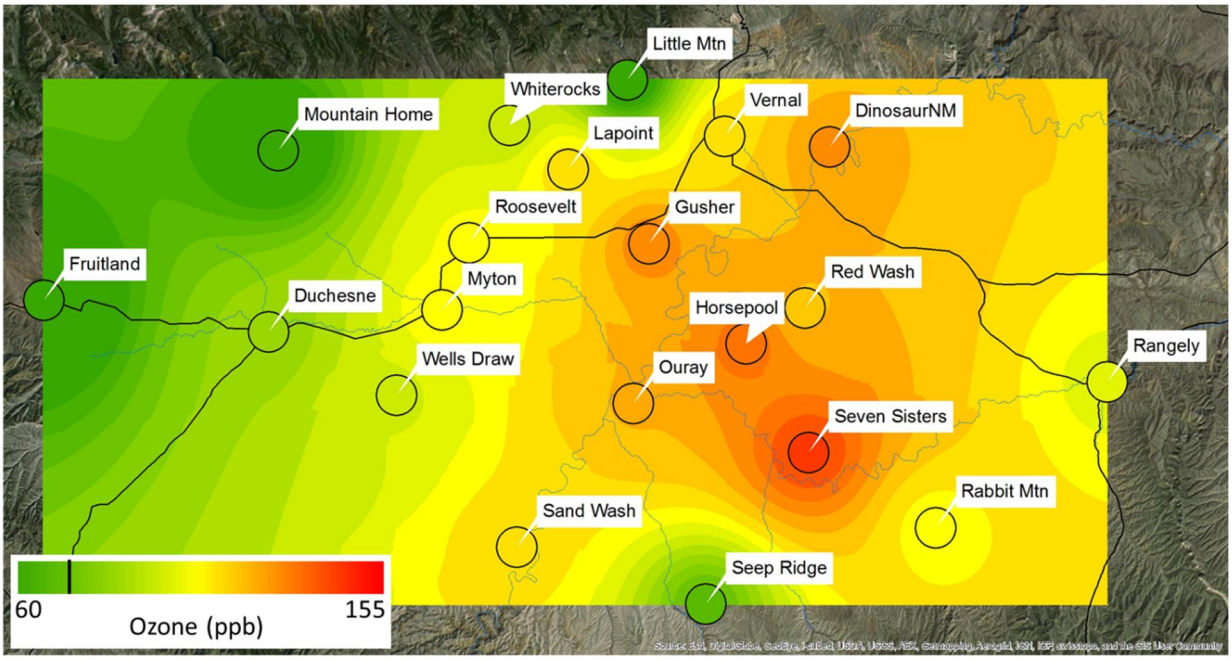

Figure 3-4. Maximum 8-hour average ozone concentrations for all sites in the Uinta Basin, 26 January.

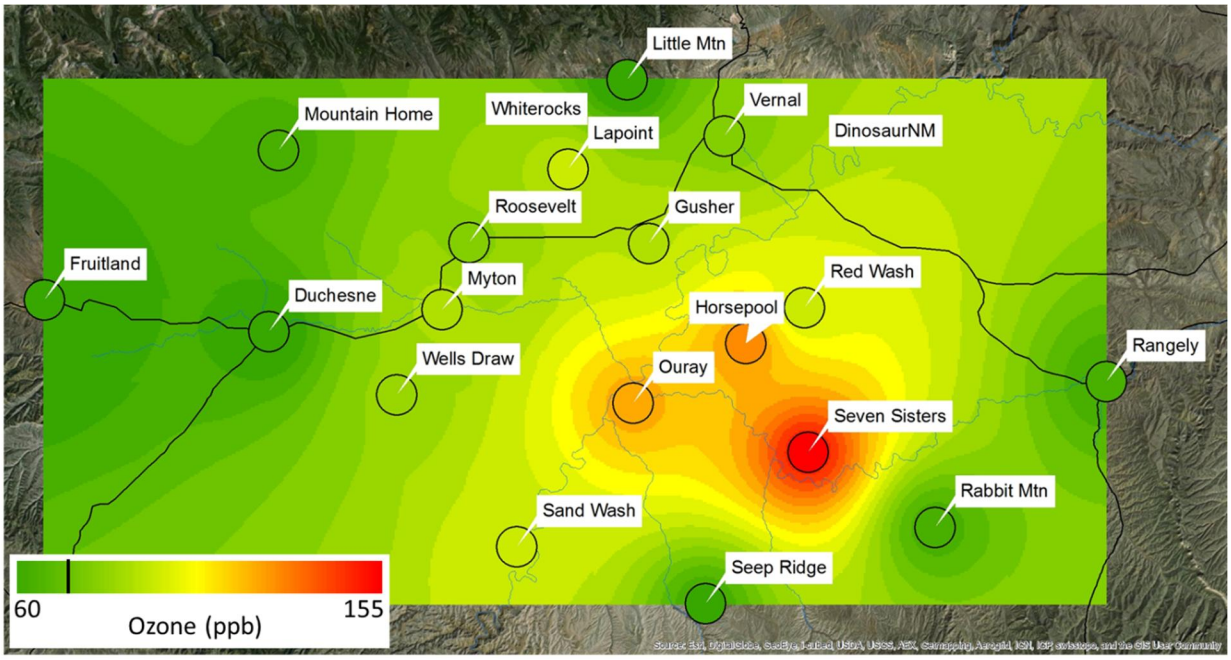

Figure 3-5. Maximum 8-hour average ozone concentrations for all sites in the Uinta Basin, 1 March.

Ozone concentrations during inversion episodes were strongly correlated with elevation, were correlated with proximity to oil and gas operations (Figure 3-6), and were less consistently correlated with other spatial metrics (Table 3-3). The correlation of ozone with oil wells was much weaker than the correlation with gas wells. Gas wells tended to be in areas of lower elevation, while oil wells did not (R^2 = 0.26, p = 0.02 for relationship between average elevation in a 25 km radius around study sites and the number of producing gas wells in the same radius), which could at least partly explain the better correlation of ozone with gas production. The average day-night difference in ozone concentration at a given site was significantly correlated with elevation and the number of people living nearby (Table 3-3).

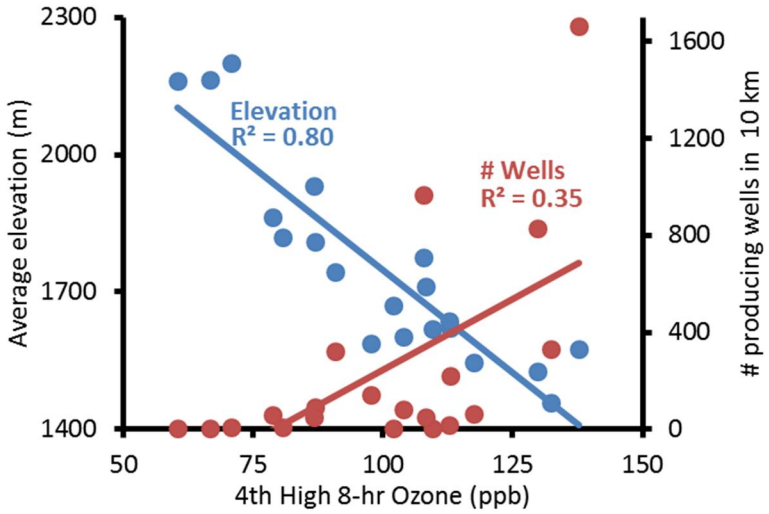

Figure 3-6. Relationship between fourth highest daily maximum 8-hr average ozone concentration for winter 2012-13 and average elevation within 10 km of a monitoring station (in blue) and number of producing oil and gas wells within 10 km of a monitoring station (in red). Linear regression lines and Pearson R^2 values are also shown.

Correlations of ozone with elevation and oil and gas production metrics were often weaker when maximum ozone on individual high ozone days, rather than ozone statistics for the whole winter season, was used (Table 3-3). For example, proximity to oil and gas production was not a significant predictor of ozone concentrations on 6 February, a day with high ozone, but it was a significant predictor on 26 January and 1 March, the days with the highest ozone values of the entire season. Correlations on 26 January and 1 March were weaker than those for the whole season. It is probable that meteorological conditions (especially air transport) on individual high ozone days obscured the impact of proximity to oil and gas production on ozone concentrations.

Correlations for spatial parameters were calculated within 5, 10, 15, 20, 25, and 50 km radii from sites, and the radii with strongest correlations are shown in Table 3-3. In general, correlations at different radii were similar to those shown, but correlations with oil and gas metrics tended to be strongest at larger radii, while correlations with population and average elevation were stronger at smaller radii.

We also explored whether the difference between the study site elevation and the average elevation of the surrounding terrain was a useful predictor of ozone concentrations. For example, the Sand Wash site was deep in the mouth of Desolation Canyon, and the average terrain in a 10 km radius around the site was 218 m higher than the elevation of the site itself. We hypothesized that sites surrounded by higher terrain would have stronger local inversion characteristics, perhaps leading to increased ozone production. No significant correlations were observed, however, between ozone concentrations and the difference between site

elevation and surrounding terrain elevation, indicating that sites in canyons or river bottoms were not more prone to ozone production than nearby areas.

Table 3-3. Pearson correlation coefficients (r) for relationships between ozone and spatial parameters. "N.S." Indicates that the correlation was not significant (α = 0.05).

	Site Elevation	Average Elevation	# Oil & Gas Wells	# Oil Wells	# Gas Wells	Monthly Oil Prod.	Monthly Gas Prod.	Population
Radius from site	**--**	**10 km**	**50 km**	**50 km**	**50 km**	**50 km**	**50 km**	**5 km**
Highest 8-hr ozone	-0.79	-0.89	0.77	N.S.	0.66	N.S.	0.65	N.S.
4th highest 8-hr ozone	-0.76	-0.90	0.75	N.S.	0.64	N.S.	0.63	N.S.
# Exceedance days	-0.75	-0.90	0.74	N.S.	0.62	N.S.	0.61	N.S.
Day-night difference ozone	-0.61	-0.54	N.S.	0.53	N.S.	0.52	N.S.	0.56
26 Jan max. 8-hr ozone	-0.84	-0.93	0.67	N.S.	0.59	N.S.	0.57	N.S.
6 Feb max. 8-hr ozone	N.S.	-0.50	N.S.	N.S.	N.S.	N.S.	N.S.	N.S.
1 Mar max. 8-hr ozone	-0.61	-0.76	0.74	N.S.	0.65	N.S.	0.65	N.S.

Multiple linear regression was employed to better understand the relationship between ozone and spatial parameters (as in Lyman and Gustin, 2009). In multiple regression analysis, a linear regression equation that incorporates more than one independent variable is used to predict the dependent variable, and the predictive value of independent variables can be individually assessed. Many of the independent variables considered in this study are correlated with each other, and the multiple regression method is able to show the value of each variable in predicting ozone concentration without the obscuring effects of this inter-correlation.

All parameters listed in the Methods section were utilized in the linear regression analysis. An iterative process of including and excluding parameters was employed to determine whether each possible independent variable added additional predictive power to the multiple regression model. Ultimately, elevation was found to be the best predictor of ozone concentration. The exact elevation of study sites was less useful, however, than the average elevation of the terrain surrounding the study sites, and average elevation in a 10 km radius of sites was the best predictor (Figure 3-6, Table 3-3).

While average elevation in a 10 km radius was able to explain 80% of the variability in the fourth highest 8-hour average ozone concentration among study sites (i.e., $R^2 = 0.80$), adding the number of producing oil and gas wells within 10 km of study sites with average elevation in a multiple regression model added 10% more predictive power (i.e., $R^2 = 0.90$). In other words, with only information about elevation and proximity to oil and gas activity, ozone concentrations during winter 2012-13 can be predicted at a given location in the Basin with 90% accuracy.

The spatial distribution of compressor stations, gas plants, and produced water impoundments was strongly correlated to that of oil and gas wells, and including these facilities in the analysis did not improve the quality of the regression. Oil production and gas production were worse predictors of ozone concentrations than the number of oil and gas wells. Using the number of gas wells within 10 km, rather than the number of oil and gas wells together, was as useful as the number of oil *and* gas wells at predicting ozone (R^2 = 0.90), but using the number of oil wells within 10 km was not (R^2= 0.81; proximity to oil wells variable was not significant, with p = 0.45). This finding could indicate that emissions associated with gas production are more important in ozone production than emissions associated with oil production, either because natural gas-related emissions are more reactive, or because they are more abundant on a per-well basis. On the other hand, the insignificance of the oil well variable could be due, at least in part, to the fact that there are fewer oil wells than gas wells in the Basin and they are less densely distributed, so with the limited number of study sites available the relationship between ozone and oil well locations was not statistically detectable. Oil wells clearly do emit NMHC and NO_x that are active in ozone production (see Section 3.1.3.2), and a similar study with more sites in the oil-producing areas of the basin may lead to a better correlation of ozone with proximity to oil wells.

While correlations of ozone with proximity to oil and gas production were strongest when larger radii were used, in the multiple regression analysis the number of wells within 10 km was the strongest predictor of ozone concentrations. While average elevation within 10 km and number of producing wells within 10 km explained 90% of the variability in fourth highest ozone, substituting the number of producing wells within 50 km allowed for explanation of only 81% of variability, and the number of wells was not a significant independent variable (p = 0.42).

Located in Colorado on the eastern edge of the Uinta Basin, the Rangely site, which is a regulatory site used by EPA to assess attainment status with respect to the NAAQS, has three years of ozone data with an average greater than 75 ppb. Some have speculated that high ozone in Rangely is due to transport of ozone and precursors from Utah (Webb, 2011). While the multi-year Uintah Basin Ozone Study (UBOS) certainly has focused on Utah (e.g., maps of oil and gas production included in the 2012 UBOS final report only showed wells in Utah), a dense field of 668 producing oil and gas wells exists within 15 km of the Rangely monitoring station (Figure 3-7). As pointed out in Section 8, Rangely is included within the region of the Basin that is below the average inversion height observed in 2013. We therefore hypothesize that some air exchange between Rangely and the Utah portion of the Uinta Basin occurs, such that ozone experienced in Rangely is due to a combination of local (i.e., within Colorado) and regional (i.e., within Utah) precursor sources.

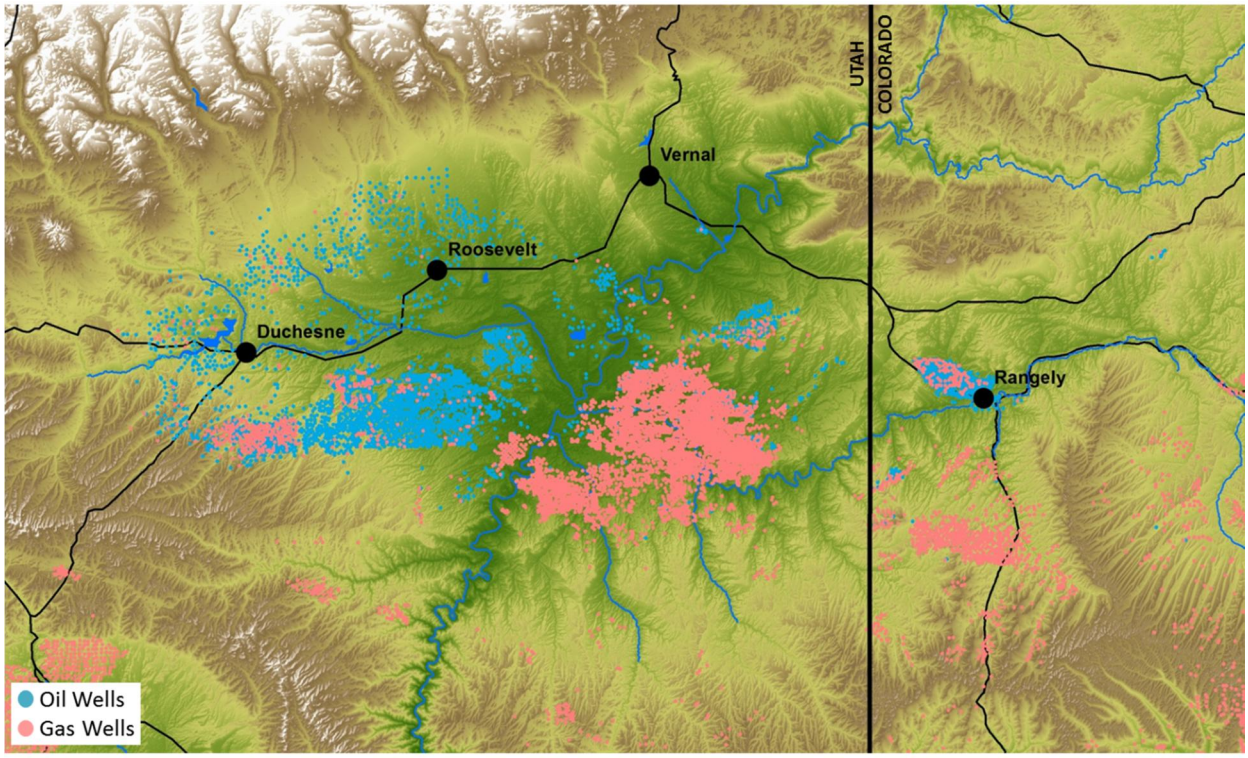

Figure 3-7. Producing oil and gas wells in and around the Uinta Basin. Wells were considered "producing" if they reported oil or gas production during February 2013.

3.1.3.2 Distribution of Nonmethane Hydrocarbons

Concentrations of NMHC[2] increased during inversion episodes, though the distribution of NMHC remained mostly the same. The highest NMHC concentrations were consistently observed at the Seven Sisters site, which is located in an area of intense natural gas production south of Vernal (Figures 3-8 and 3-9). At the height of an inversion episode on 6 February, the distributions of alkanes and aromatic compounds were similar, with highest concentrations at the Seven Sisters and Horsepool sites, followed by Roosevelt, and then by Vernal and Wells Draw (Figure 3-9). Fruitland, a site remote from oil and gas activity on the western edge of the Uinta Basin, consistently had the lowest NMHC concentrations. This spatial distribution of NMHC was similar to observations during non-inversion conditions during winter 2011-12 (Lyman et al., 2013).

[2] The term "VOC" usually omits methane and ethane since they are less reactive than most other volatile organics, while "NMHC" refers to *all* nonmethane organics, regardless of reactivity.

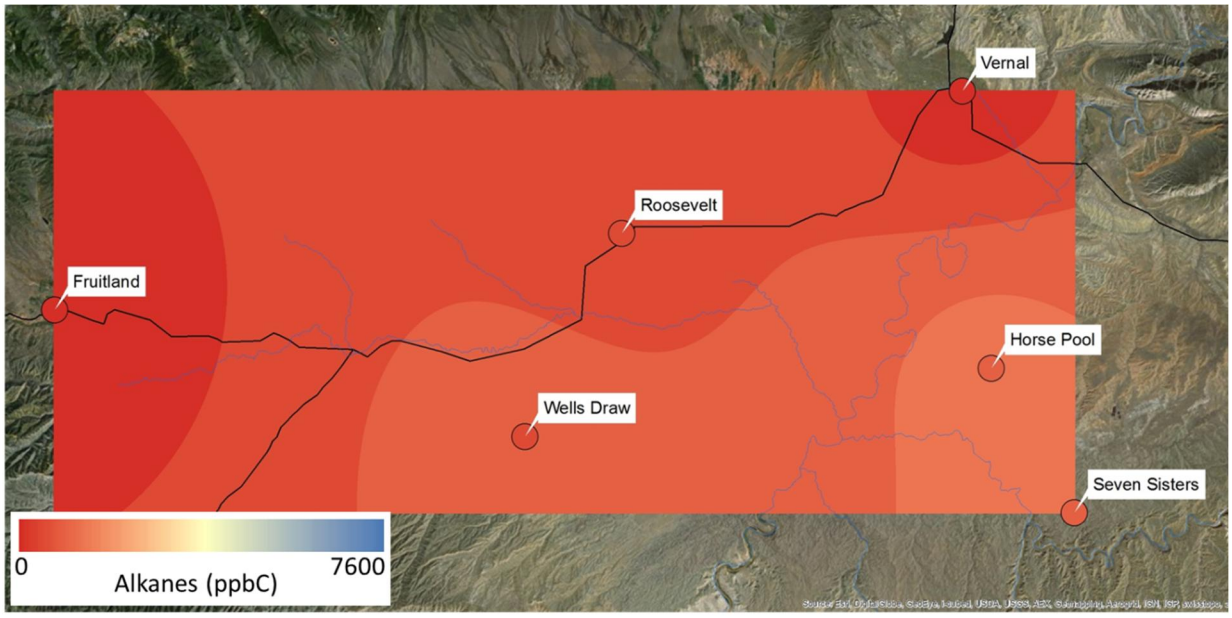

Figure 3-8. Sum of all alkanes measured on 1 February (the start of an inversion episode) at six sites around the Uinta Basin.

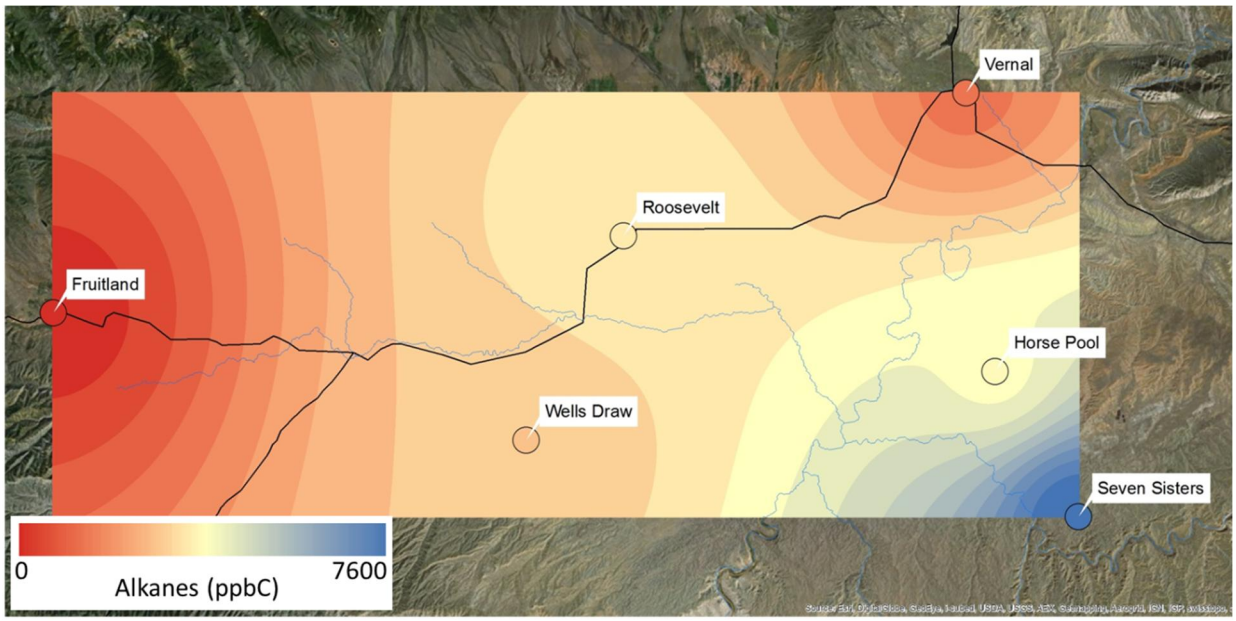

Figure 3-9. Sum of all alkanes measured on 6 February (day of highest ozone during the inversion episode noted in previous figure) at six sites around the Uinta Basin.

The ratio of alkanes to aromatics was higher at Wells Draw, a site in an area of intense oil production, than at Seven Sisters, a site in an area of mostly gas production, echoing observations made during non-inversion conditions in winter 2011-12 (Lyman et al., 2013). Alkene concentrations were also highest at Wells Draw (Figure 3-11). The source of higher

alkenes in this oil producing region is uncertain, though fuel combustion is known to be an important source of alkenes (Doskey et al., 1992), and pump jack engines in this area may be a significant alkene source. Methanol distribution was similar to alkane distribution (Figure 3-12).

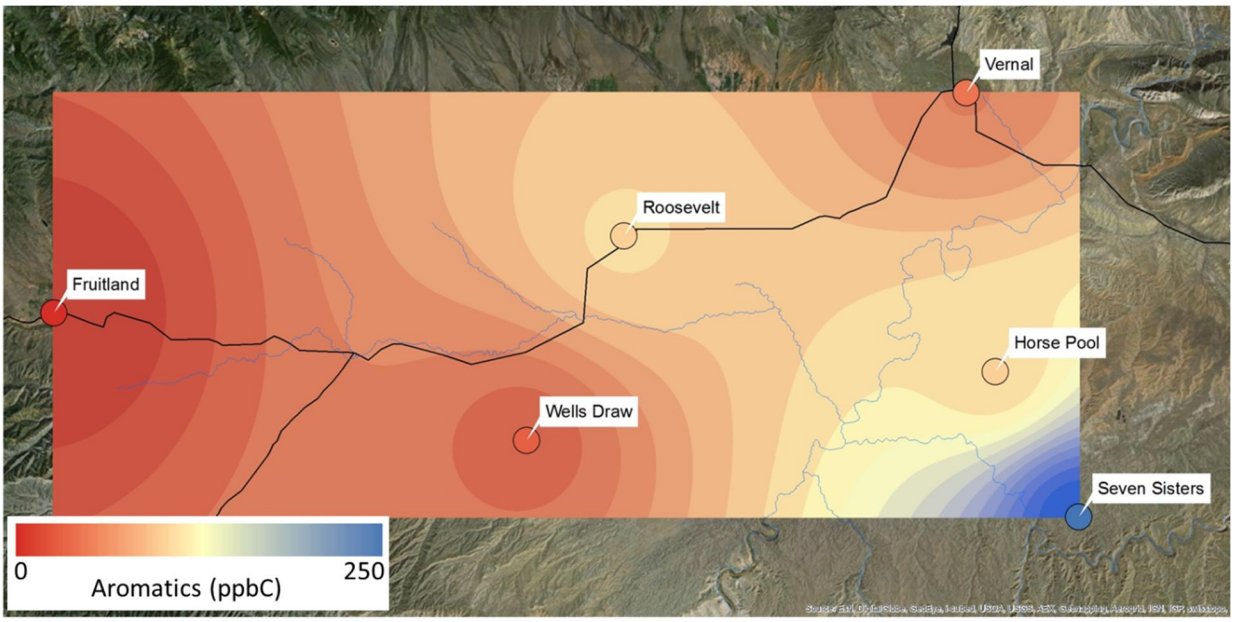

Figure 3-10. Sum of all aromatics measured on 6 February (day of highest ozone during an inversion episode) at six sites around the Uinta Basin.

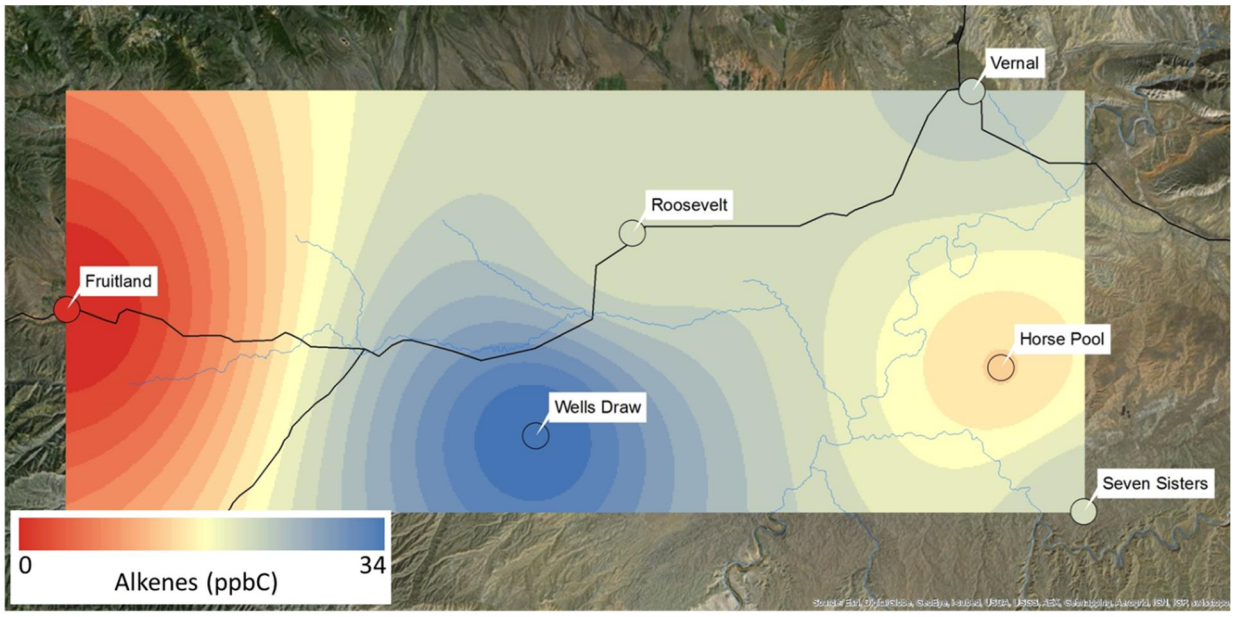

Figure 3-11. Sum of all alkenes measured on 6 February (day of highest ozone during an inversion episode) at six sites around the Uinta Basin.

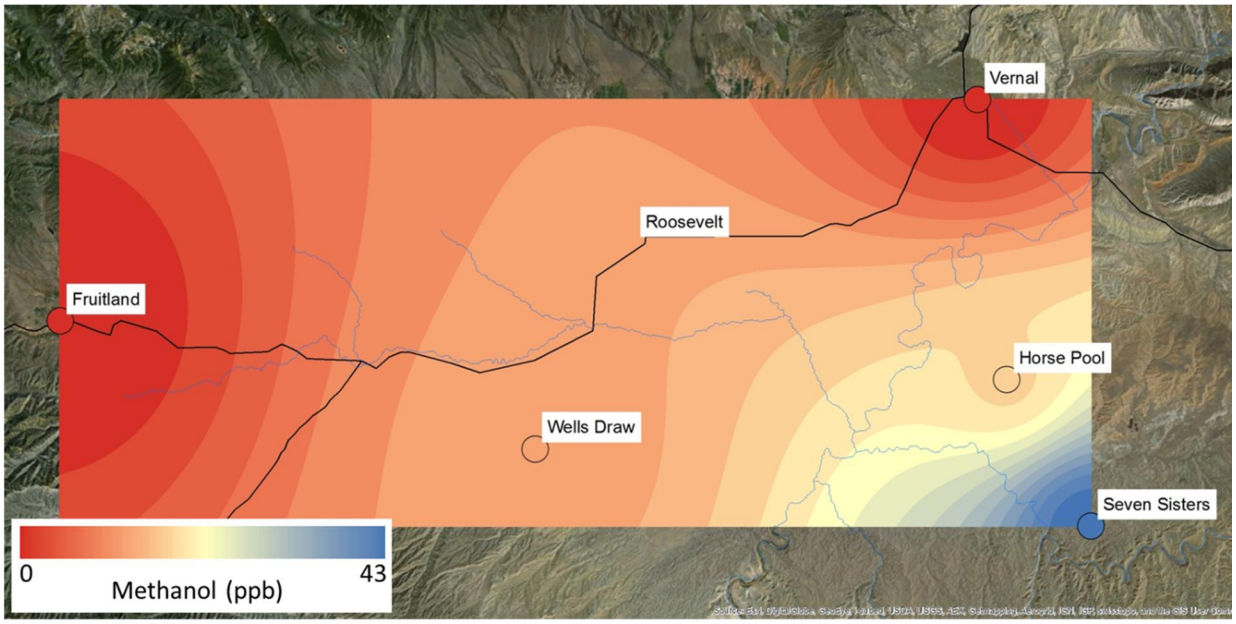

Figure 3-12. Methanol measured on 6 February (day of highest ozone during an inversion episode) at five sites around the Uinta Basin.

Different NMHC have different reactivities (i.e., different ability to produce ozone). The ability of VOC to produce ozone can be measured via Maximum Incremental Reactivity (MIR; Carter, 2009). MIR uses box model simulations parameterized to maximize the sensitivity of ozone production to changes in NMHC concentrations. An MIR for a compound is the unit change in ozone production that occurs with a corresponding change in that compound. Since NMHC speciation is different at different sites around the Uinta Basin, MIR can provide a more useful means than NMHC abundance alone to determine the potential of NMHC to form ozone at various study sites. Ideally, MIR scales should be developed using meteorological and other conditions specific to the study area, but this is not yet feasible for the Uinta Basin because of uncertainties in wintertime ozone chemistry. In this work, we use the MIR scale from Carter (2009) as an approximation for MIR in the Uinta Basin during winter inversion conditions.

In Table 3-4, NMHC concentrations and corresponding MIR are shown for 6 February, the highest ozone day during an inversion episode that occurred during the first eight days of February. MIR are shown in units of µg of ozone produced per cubic meter of air. These values were derived by multiplying the concentration of individual compounds (units of µg per m^3 of air) by the MIR for that compound (units of µg of ozone produced per µg of the organic compound under consideration) and indicate the maximum amount of ozone that could be produced from that amount of NMHC. Two µg O_3 m^{-3} are approximately equivalent to 1 ppb of ozone.

Table 3-4. NMHC concentrations and MIR for six sites in the Uinta Basin on 6 February.

		Horsepool	Vernal	Wells Draw	Fruitland	Seven Sisters	Roosevelt
Concentrations							
Alkanes	ppbC	3847.9	1428.4	2829.7	168.5	7679.9	3548.5
Alkenes	ppbC	14.4	22.7	34.6	<2.0	21.8	20.2
Aromatics	ppbC	105.0	54.8	36.0	7.2	251.9	107.3
Alkanes	ppbv	2283.9	847.4	1699.4	100.7	4519.6	2117.1
Alkenes	ppbv	9.9	14.3	19.5	<1.0	16.9	12.4
Aromatics	ppbv	55.4	28.2	18.4	3.9	134.1	56.5
Methanol	ppbv	23.4	<5	16.2	<5	57.5	--
Ethane	ppbv	202.4	65.6	145.9	8.1	370.9	153.7
Maximum Incremental Reactivities							
All NMHC	µg O_3 m^{-3}	1917.3	827.6	1406.6	86.7	4076.6	1839.6
Alkanes	µg O_3 m^{-3}	1649.8	633.4	1206.0	74.9	3405.5	1505.4
Alkenes	µg O_3 m^{-3}	51.5	85.7	119.2	<10	105.2	104.7
Aromatics	µg O_3 m^{-3}	203.1	109.3	69.3	11.8	541.9	230.3
Methanol	µg O_3 m^{-3}	15.2	<4	10.5	<4	37.4	--
Ethane	µg O_3 m^{-3}	202.4	65.6	145.9	8.1	370.9	153.7
Alkanes	% of total	86.05	76.54	85.74	86.42	83.54	81.83
Alkenes	% of total	2.69	10.36	8.48	<10	2.58	5.69
Aromatics	% of total	10.59	13.21	4.93	13.58	13.29	12.52
Methanol	% of total	0.79	<0.5	0.75	<0.5	0.92	--
Ethane	% of total	10.56	7.93	10.37	9.31	9.10	8.36

At every site, including Fruitland, NMHC was comprised mostly of alkanes, and alkanes made up the majority of total MIR. In other words, the majority of ozone at the sites can be expected to have been produced from reactions involving alkanes. The percentage of total MIR attributable to aromatics and alkenes varied somewhat among sites. Aromatics contributed more than 10% of MIR at all sites except Wells Draw, and Vernal, Roosevelt, and Wells Draw were the only sites with more than 3% of MIR due to alkenes. Methanol contributed less than 1% of total MIR in all cases, while ethane, often considered too unreactive to regulate (EPA, 2003), made up 7-11% of total MIR at the study sites.

Because such a large percentage of NMHC in the Uinta Basin is alkanes (95-97% as ppbC at the six sites in this study), these compounds make up the vast majority of total MIR, even though they are low on the MIR scale relative to alkenes and most aromatics. Thus, while emissions controls that focus on aromatics and alkenes because of their high reactivity may produce more benefit at a lower cost, focus on highly reactive VOC alone is not likely to be adequate to control ozone pollution in the Basin.

Though only six distributed NMHC monitoring stations existed during winter 2012-13, statistically significant correlations were observed with a number of spatial and other variables. Figure 3-13 shows that the same predictors of ozone concentrations (area average elevation and proximity to oil and gas activity) were also strong predictors of NMHC. Alkanes, aromatics, and methanol were all strongly correlated with each other, with total NMHC, and with ozone

(Table 3-5, Figure 3-14). Alkenes, on the other hand, exhibited few significant correlations, owing to their dramatically different distribution relative to other NMHC categories (Figure 3-11). Alkenes were correlated with proximity to oil wells, indicating that processes associated with oil production may be larger sources of alkenes than processes associated with natural gas production.

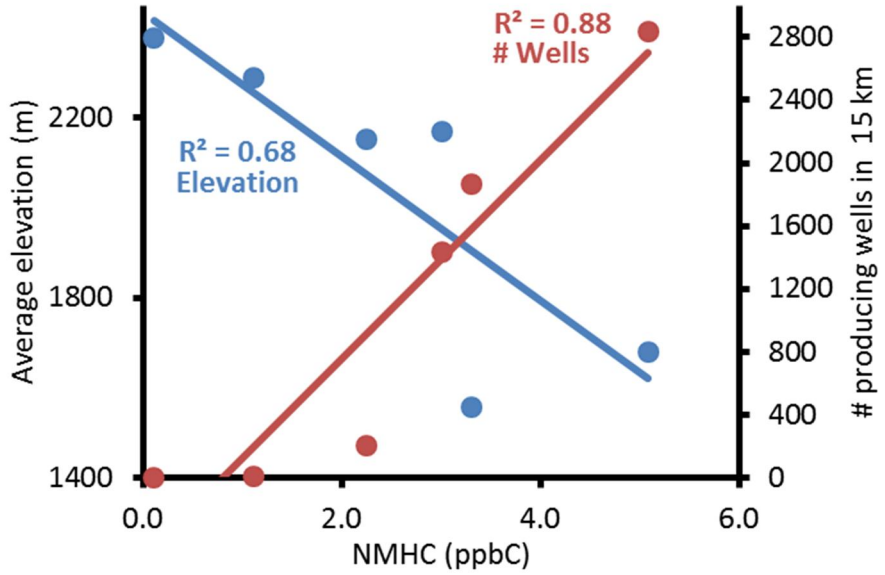

Figure 3-13. Relationship between 1-8 February average total NMHC concentration and average elevation within 25 km of monitoring stations (in blue) and number of producing oil and gas wells within 15 km of monitoring stations (in red). Linear regression lines and Pearson R^2 values are also shown.

Table 3-5. Pearson correlations (r) for average NMHC concentrations for 1-8 February at the six sites shown in Table 3-4. "N.S." Indicates the correlation was not significant (α = 0.10).

	NMHC (ppbC)	Alkanes (ppbC)	Alkenes (ppbC)	Aromatics (ppbC)	Methanol (ppbv)
Alkanes (ppbC)	0.99	--	N.S.	0.80	0.96
Alkenes (ppbC)	N.S.	N.S.	--	N.S.	N.S.
Aromatics (ppbC)	0.82	0.80	N.S.	--	0.81
Methanol (ppbv)	0.95	0.96	N.S.	0.81	--
Highest 8-hr ozone	0.92	0.90	N.S.	0.81	0.81
4th highest 8-hr ozone	0.92	0.91	N.S.	0.87	0.86
26 Jan max. 8-hr ozone	0.81	N.S.	N.S.	0.91	N.S.
6 Feb max. 8-hr ozone	0.84	0.86	N.S.	N.S.	N.S.
1 Mar max. 8-hr ozone	0.93	0.91	N.S.	0.93	0.95
# Wells in 15 km	0.94	0.91	N.S.	0.73	0.98
# Oil wells in 15 km	N.S.	N.S.	0.73	N.S.	N.S.
# Gas wells in 15 km	0.84	0.81	N.S.	0.85	0.96
Population in 15 km	N.S.	N.S.	N.S.	N.S.	N.S.
Avg. elevation in 25 km	-0.83	-0.82	N.S.	-0.75	-0.93

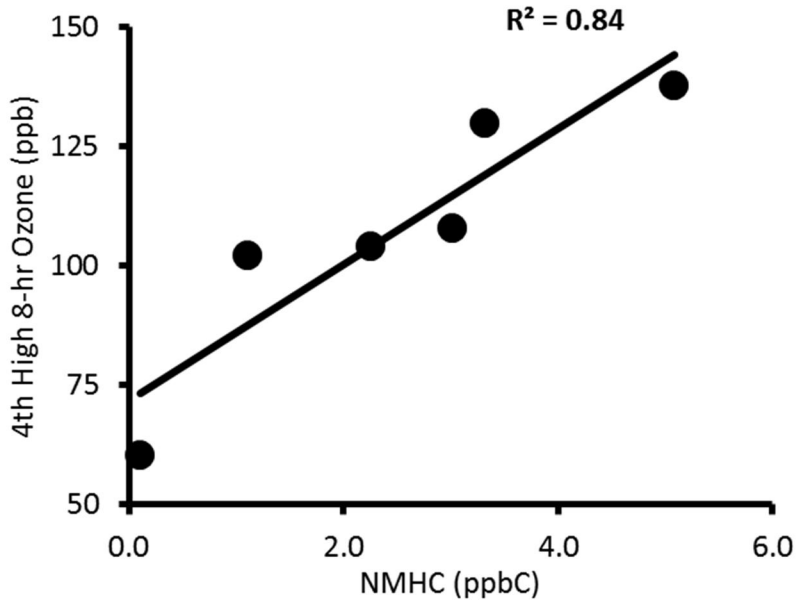

Figure 3-14. Relationship between 1-8 February average total NMHC concentration and fourth highest 8-hour ozone concentration at study sites. A linear regression line and Pearson R^2 value is also shown.

3.1.3.3 Distribution of Oxides of Nitrogen

Figures 3-15 through 3-17 show the distribution of NO_x during three inversion episodes. NO_x tended to be highest in populated areas and areas with more natural gas production, especially the Seven Sisters site, which is in the area of maximum well density in the Basin and is near several large compressor stations and gas plants.

In general, NO_x concentrations were highest during January inversion episodes and decreased as the winter progressed. The lapse rate in the Uinta Basin was most negative (indicating that inversions were stronger) in January and became less negative as the winter progressed (Figure 3-2). The stronger inversions in early winter likely were more effective at trapping ozone precursors, while stronger solar radiation later in winter likely inhibited inversion formation and allowed for more dilution of emitted precursors.

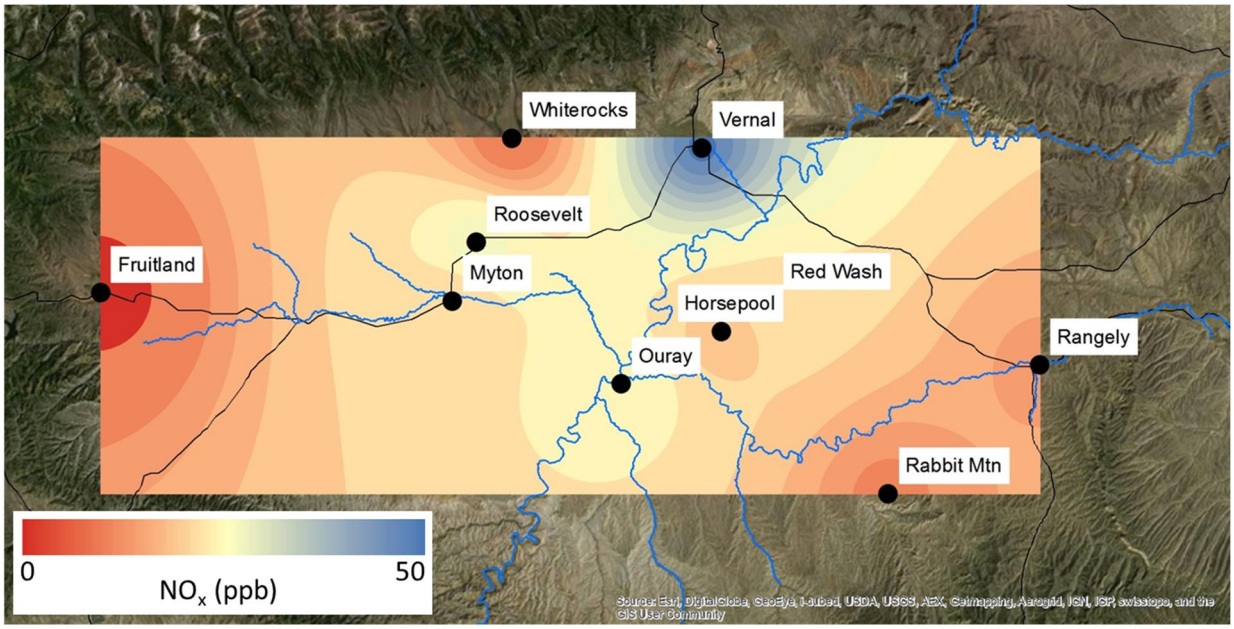

Figure 3-15. Average NO_x at ten sites during an inversion episode that occurred 20-26 January.

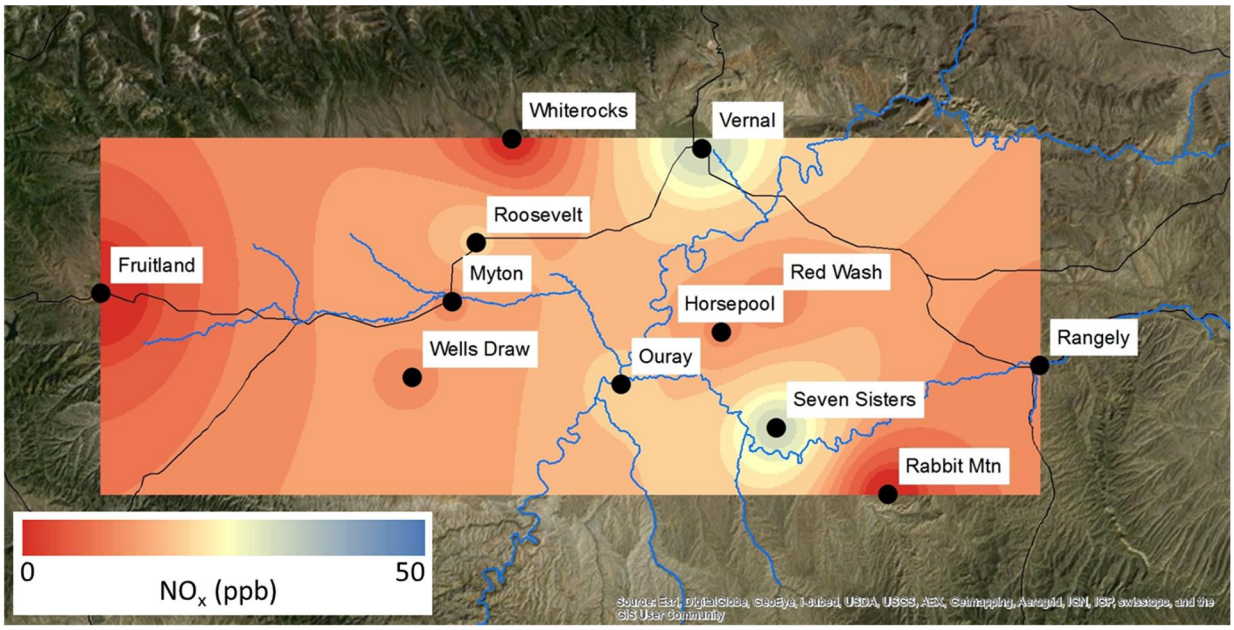

Figure 3-16. Average NO_x at twelve sites during an inversion episode that occurred 30 January through 5 February. NO_x concentrations shown for Wells Draw and Seven Sisters are derived from passive Radiello samplers.

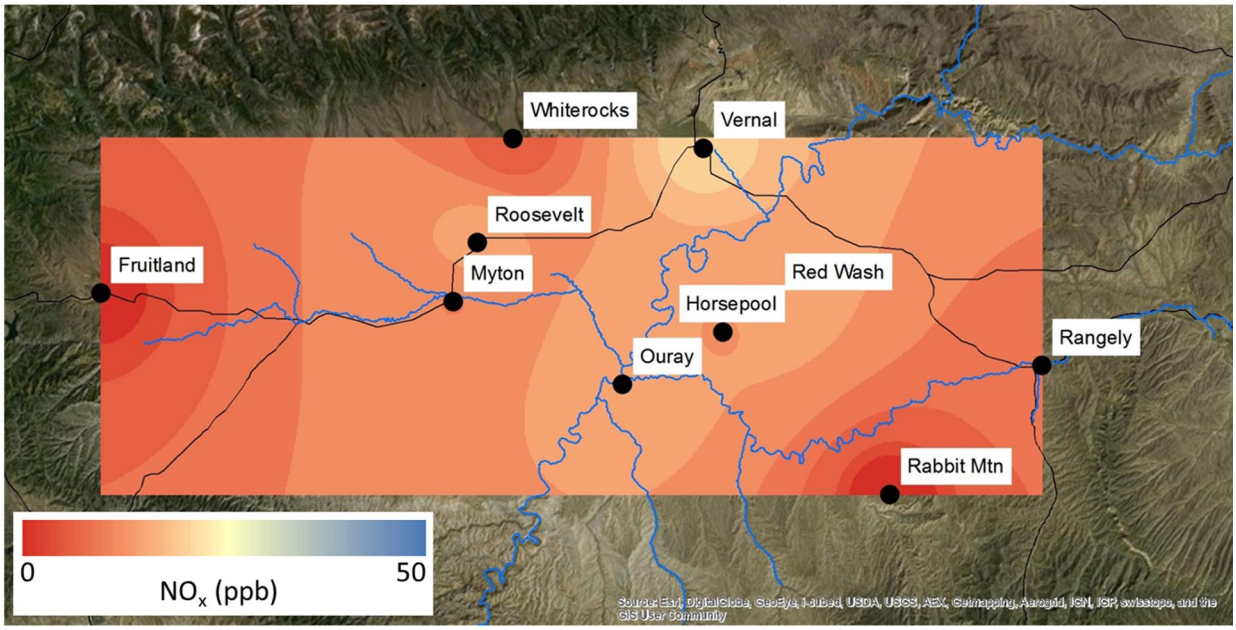

Figure 3-17. Average NO_x at ten sites during an inversion episode that occurred 1-3 March.

NO_x concentrations at most sites were collected with instruments that utilize molybdenum oxide converters to transform NO_2 to NO. Because these converters also transform some NO_y (i.e., the sum of all reactive nitrogen compounds, including NO and NO_2, HNO_3, HONO, particulate nitrogen, and other compounds) to NO, the NO_2 and NO_x values obtained from these instruments were biased (high). Since the NO_x analyzer at Horsepool utilized a photolytic NO_2 converter that does not transform NO_y, NO_2 concentrations at that site were not biased.

Since different sites may not have the same ratio of NO_x to NO_y, correcting NO_x values collected with molybdenum converters to true NO_x, or vice versa, is problematic. Fortunately, molybdenum converter NO_x measurements were collected at Horsepool by the University of Colorado (CU research group of D. Helmig; instrument provided by Utah Department of Environmental Quality) from 1 through 18 February, and we were able to conduct a comparison of the two methods. The molybdenum converter-based instrument pulled air from 2 m above ground, while the USU instrument pulled from 4 m above ground, and the two inlets were about 50 m apart. Figures 3-18 and 3-19 show that NO concentrations measured by the two systems were comparable, but NO_x concentrations were very different and were relatively weakly correlated. Figure 3-20 shows that the molybdenum converter-based NO_x measurement was better correlated with NO_y than with true NO_x.

NO_y concentrations at Horsepool, and presumably at sites throughout the Uinta Basin, were much higher than true NO_x during inversion episodes, and the NO_x concentrations presented in Figures 3-15 through 3-17 should be interpreted as NO_x + some portion of NO_y. For Figures 3-15 through 3-17, NO_x at Horsepool was calculated based on the relationship between measured NO_y and molybdenum converter NO_x. In Figure 3-16, NO_x for the Wells Draw and Seven Sisters sites was calculated based on the relationship between true NO_2 measurements collected by

Radiello passive samplers and molybdenum converter NO_x measurements at Fruitland, Vernal, and Horsepool.

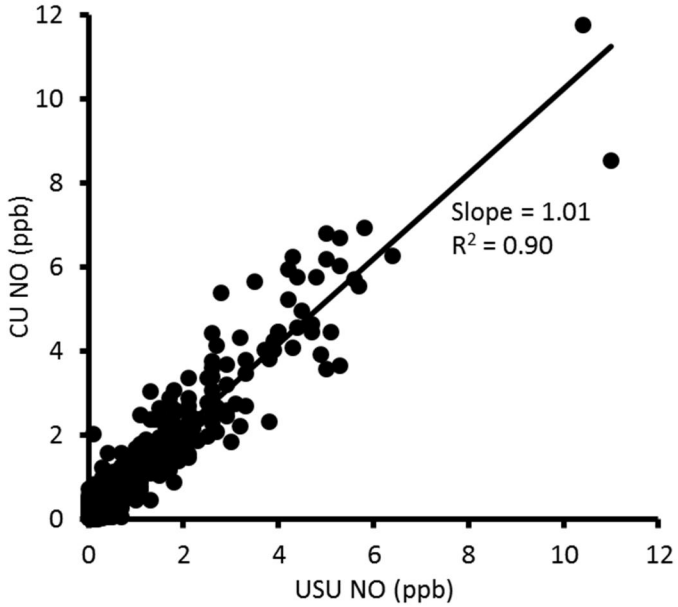

Figure 3-18. Comparison of NO measured by a photolytic NO_x analyzer (USU) to a molybdenum converter-based NO_x analyzer (CU). The linear regression curve, R^2 value, and slope of the relationship are also shown.

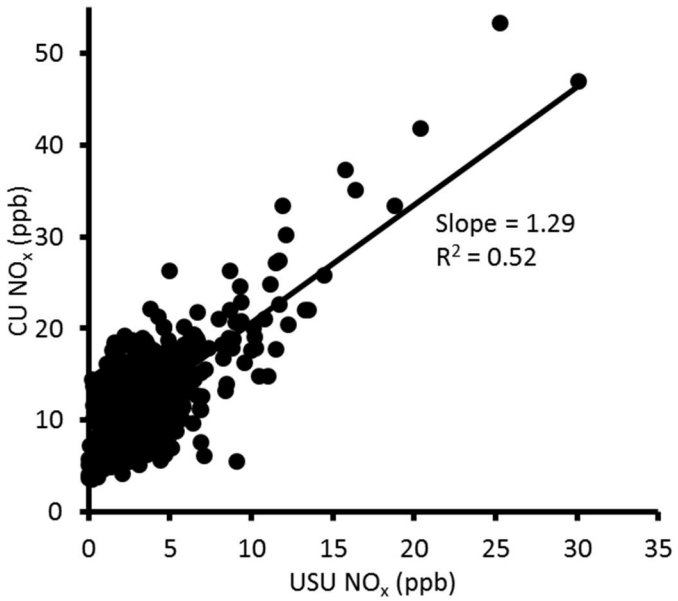

Figure 3-19. Comparison of NO_x measured by a photolytic NO_x analyzer (USU) with a molybdenum converter-based NO_x analyzer (CU). The linear regression curve, R^2 value, and slope of the relationship are also shown.

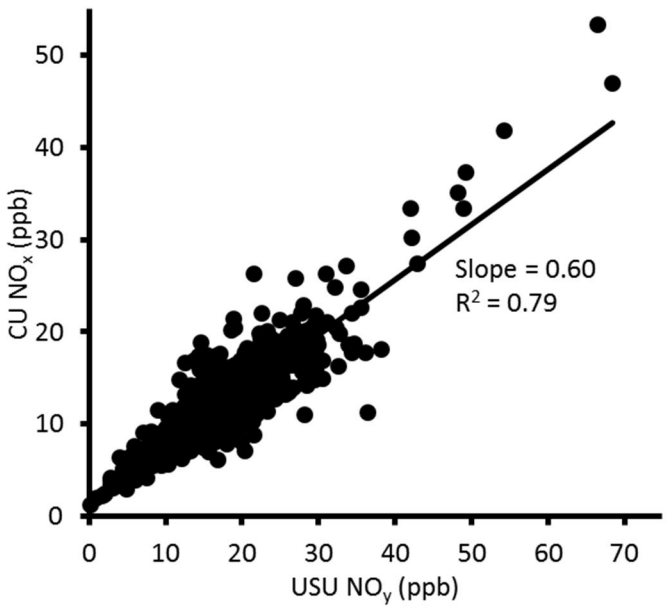

Figure 3-20. Comparison of NO_y (USU) with NO_x measured by a molybdenum converter-based NO_x analyzer (CU). The linear regression curve, R^2 value, and slope of the relationship are also shown.

NO_x concentrations at Vernal and Roosevelt were among the highest observed at any study site and exhibited the largest diurnal changes, with highest NO_x in the morning hours (Figure 3-21), likely due to diurnal traffic patterns in these cities. Red Wash, located only 250 m from a well-traveled highway, also showed significant diurnal variability, but the peak NO_x at Red Wash was at midday. NO_x also peaked at midday at the Ouray and, to some extent, Horsepool sites, similar to observations made during winter 2011-12 (Lyman et al., 2013). A counter at the Horsepool site during winter 2011-12 observed highest traffic at midday.

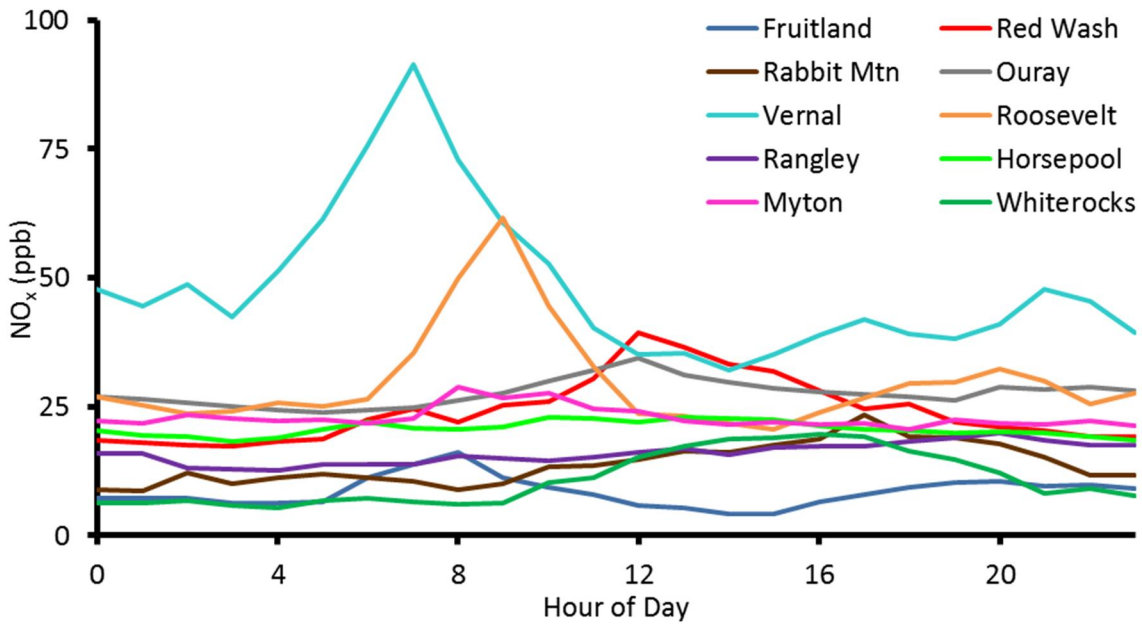

Figure 3-21. Diurnal change in NO_x concentrations at 10 sites around the Uinta Basin during the 20-26 January inversion episode.

Table 3-6 and Figure 3-22 show that the spatial distribution of NO_x was, in some instances, correlated with the spatial distribution of ozone. This relationship was not significant for the distribution of NO_x over the entire study period, but was significant for NO_x distribution during some inversion episodes. NO_x distribution was strongly correlated with the difference between day and night ozone concentrations, probably because ozone can be destroyed by NO at night, and sites with high NO_x also tend to be sites with higher nighttime NO. Correlations between NO_x concentrations and proximity of study sites to oil and gas operations were either not significant or weak, but NO_x was correlated with population and elevation.

NO_x concentrations during the 31 January through 5 February period were not significantly correlated with total NMHC measured during the same period ($p = 0.391$), but they were correlated with aromatics ($R^2 = 0.61$, $p = 0.07$). When 1-8 February average NMHC and 31 January through 5 February NO_x were used as independent variables to predict 6 February ozone in a multiple linear regression model, the NO_x variable was not significant ($p = 0.77$). However, the tendency of NO_x to destroy ozone under some conditions may have confounded this relationship, and, as discussed previously, NO_x measurements used here also contain NO_z compounds that are not direct ozone precursors. In addition, ozone production has a non-linear dependence on NO_x concentration, so a linear regression model cannot reliably evaluate the relationship of ozone to NO_x.

Table 3-6. Pearson correlations (r) of average NO_x during different periods with ozone and spatial metrics. "N.S." Indicates that the correlation was not significant (α = 0.10).

	Avg. NO_x 20-26 Jan.	Avg. NO_x 1-3 Mar.	Avg. NO_x 31 Jan.-5 Feb.	Avg NO_x 15 Jan.-10 Mar.
Highest 8-hr ozone	N.S.	0.63	0.62	N.S.
4th highest 8-hr ozone	N.S.	0.73	0.65	N.S.
# Exceedance days	N.S.	0.77	0.57	0.56
Day-night difference ozone	0.88	0.78	0.81	0.86
26 Jan max. 8-hr ozone	N.S.	N.S.	0.68	N.S.
6 Feb max. 8-hr ozone	N.S.	0.67	0.50	N.S.
1 Mar max. 8-hr ozone	N.S.	N.S.	0.59	N.S.
# wells in 5 km	N.S.	N.S.	0.51	N.S.
Population in 5 km	0.83	0.64	0.57	0.82
Avg. elevation in 5 km	-0.65	-0.79	-0.64	-0.64

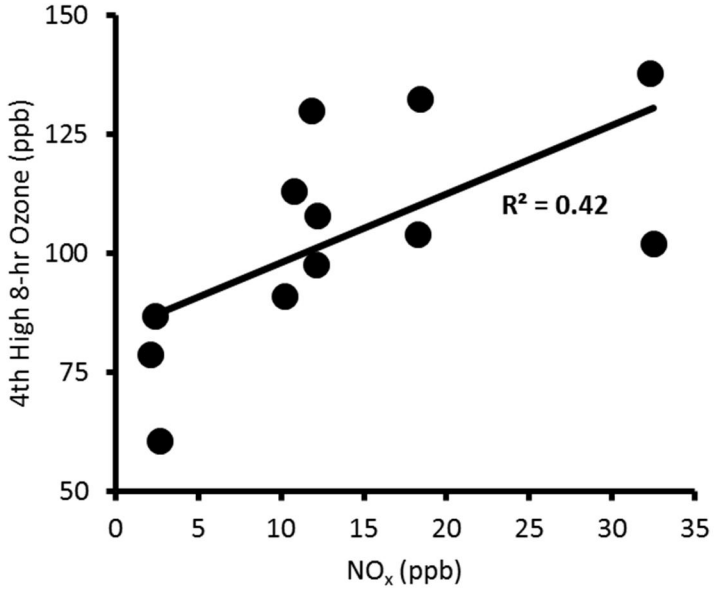

Figure 3-22. Relationship between 31 January through 5 February molybdenum converter-based NO_x concentration (contains some NO_y) and fourth highest 8-hour ozone concentration at 12 study sites. A linear regression line and Pearson R^2 value are also shown.

3.1.3.4 Influence of Transport Patterns on Ozone During an Inversion Episode

UBOS study participants and others operated dozens of meteorological stations in and around the Uinta Basin during winter 2012-13. Meteorology, particularly wind speed and direction, was an important determinant of ozone production in the Basin. Figures 3-23, 3-24, and 3-25 show ozone concentrations and wind vectors prior to and during an inversion episode that occurred from 31 January through 8 February.

Figure 3-23 shows wind conditions and the low ozone concentrations of 28 January, just two days after one of the season's highest ozone days in the Basin. A storm front arrived on 27 and 28 January and was associated with relatively high winds in many parts of the Basin on 28 January, as shown. Winds at high elevation sites during this period were from the south. Wind speeds within the Basin were lower on subsequent days, allowing another inversion to form and ozone concentrations to rebuild. By the afternoon of 6 February (Figure 3-24), ozone concentrations exceeded 100 ppb at many sites. Wind at high elevations continued to be from the south throughout this period, and wind at lower elevation sites in the Basin was light and variable (Figure 3-24). On 8 February, however, wind at high elevation sites changed directions and blew from the north (Figure 3-25). Following this synoptic scale change, wind at low elevation sites within the Basin continued to be light and variable, but a partial mix-out of ozone from the Basin nevertheless occurred, and ozone concentrations dropped to less than 100 ppb at all sites.

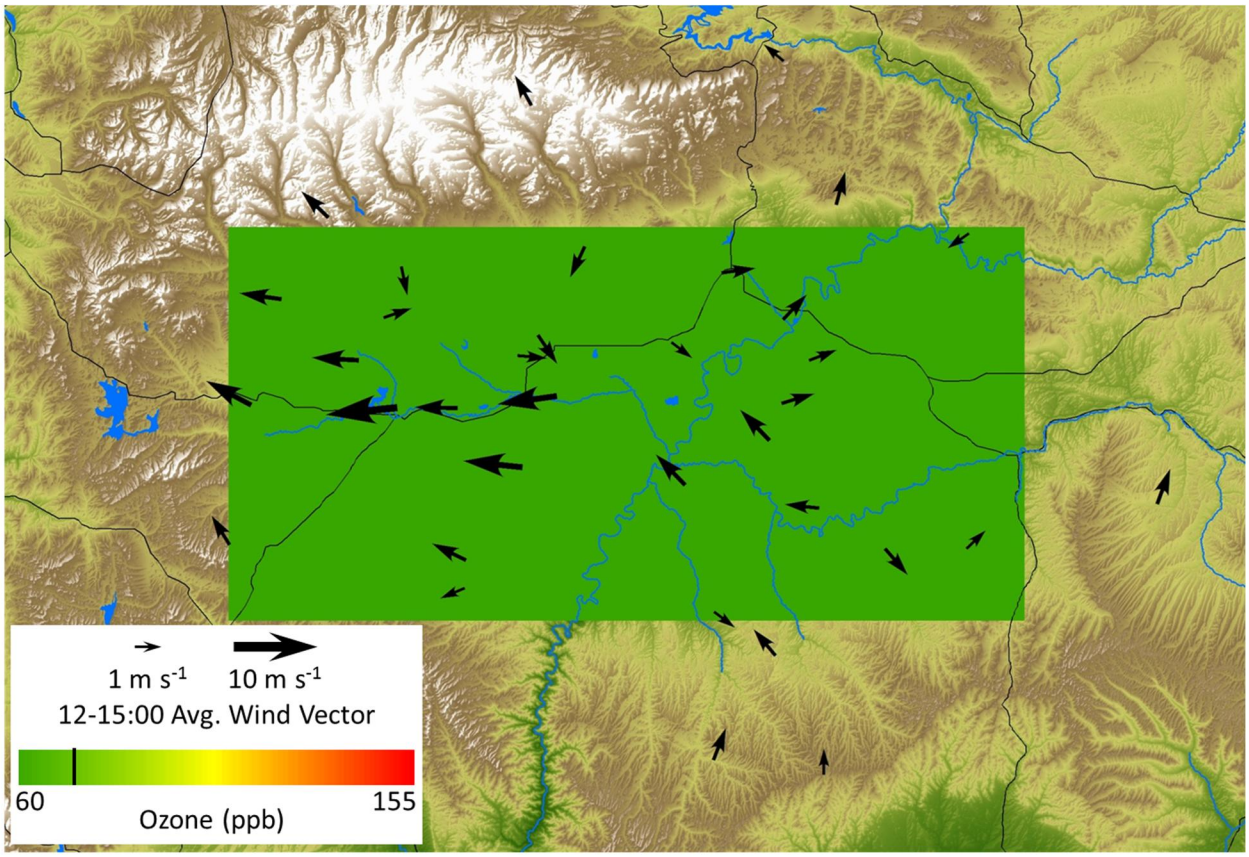

Figure 3-23. Daily maximum ozone concentrations and wind vectors from surface sites on 28 January during a stormy period between inversion episodes. Arrows indicate wind direction. The black line on the ozone color scale indicates 75 ppb.

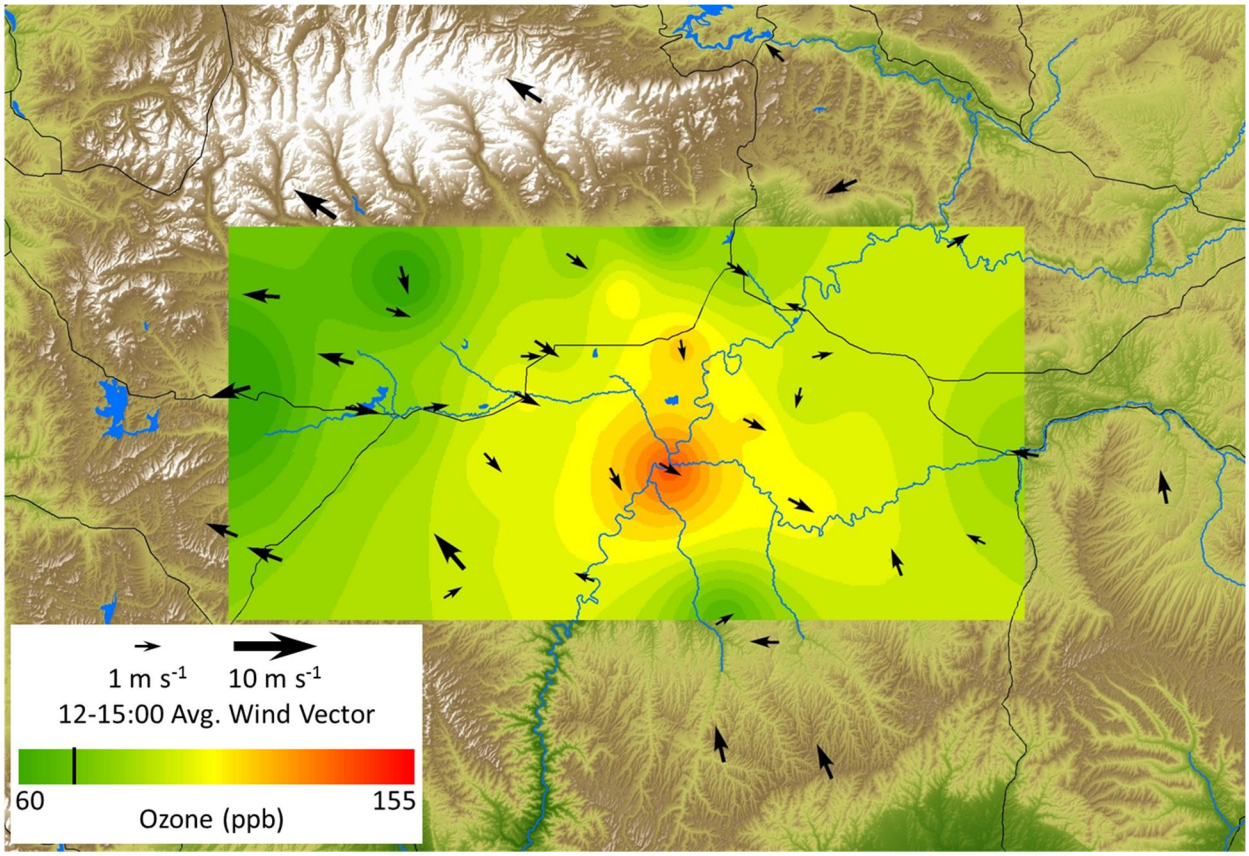

Figure 3-24. Daily maximum ozone concentrations and wind vectors from surface sites on 6 February during an inversion episode.

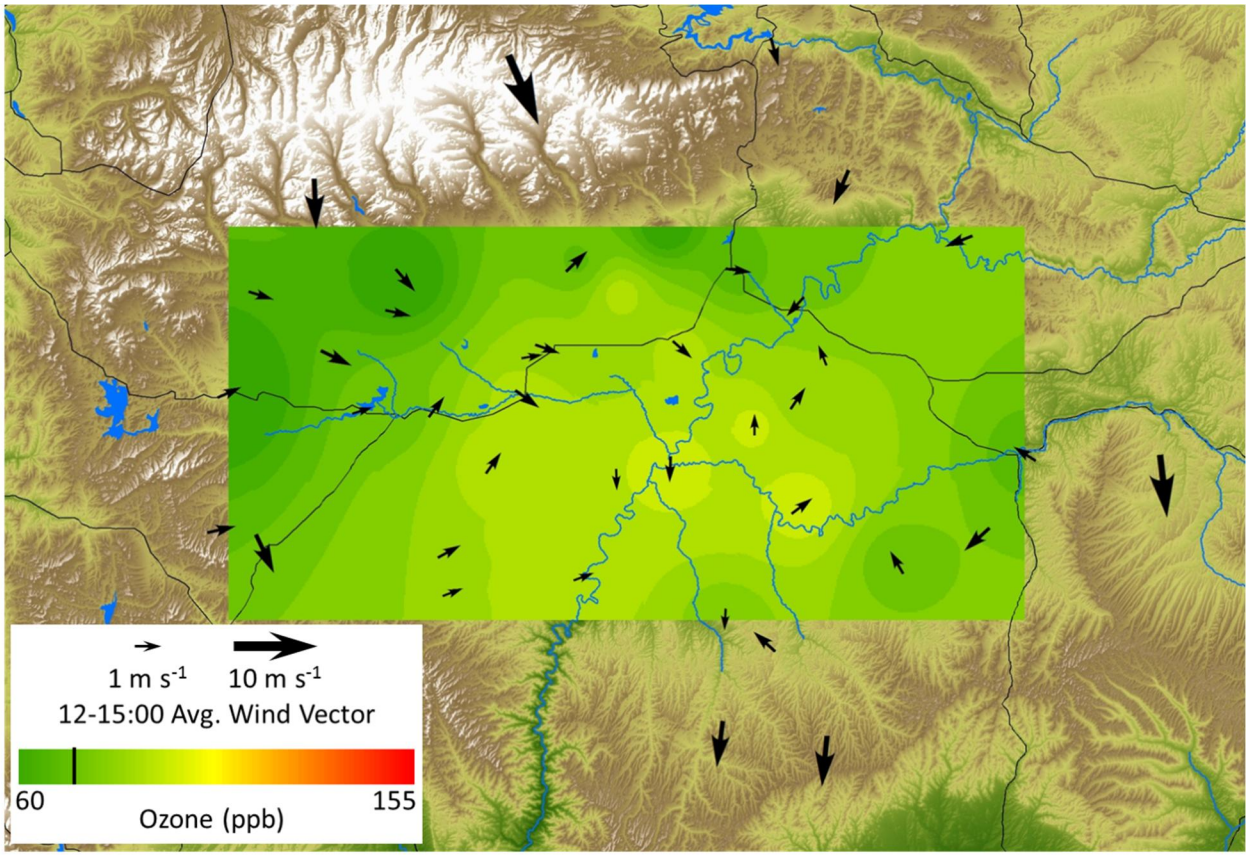

Figure 3-25. Daily maximum ozone concentrations and wind vectors from surface sites on 8 February.

3.1.3.5 Seasonal Changes in Ozone and Precursor Chemistry

While inversions became weaker (less negative lapse rate) as the winter ozone season proceeded from January through March, maximum ozone concentrations increased and took fewer inversion days to reach maxima (Figure 3-2). Figures 3-26, 3-27, and 3-28 show average ozone and precursor concentrations for each hour of the day during three inversion episodes that occurred in January, February, and March. Concentrations of ozone precursors decreased with each successive episode, but the amount of ozone produced each day (i.e., the difference between morning and afternoon ozone concentrations) increased. Average total NMHC (TNMHC) was 37% lower during 1-3 March than during 20-26 January, and NO_2 was 63% lower, but daily ozone production was 64% higher during 1-3 March than during the earlier period. The average daytime total UV radiation (average of the sum of incoming and outgoing UV-A and UV-B for daylight hours) was 51% higher during 1-3 March, and daily maximum temperature was 10.5 °C higher, probably accounting for the observed increase in daily ozone production.

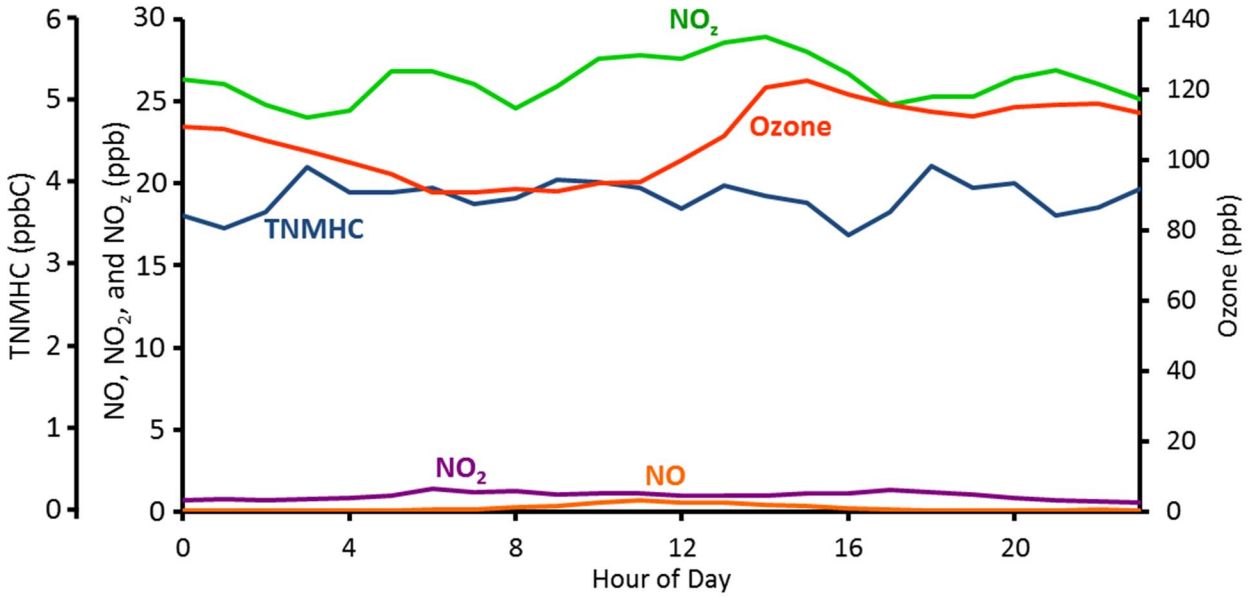

Figure 3-26. Diurnal average concentrations of ozone and precursors at Horsepool, 20-26 January.

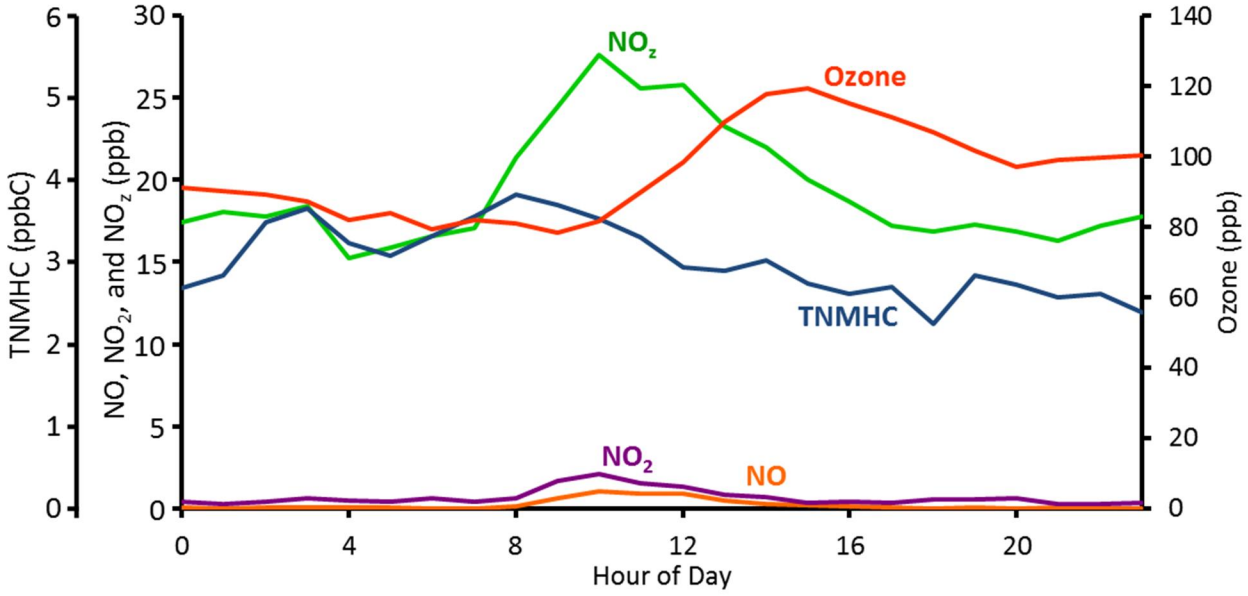

Figure 3-27. Diurnal average concentrations of ozone and precursors at Horsepool, 4-6 February.

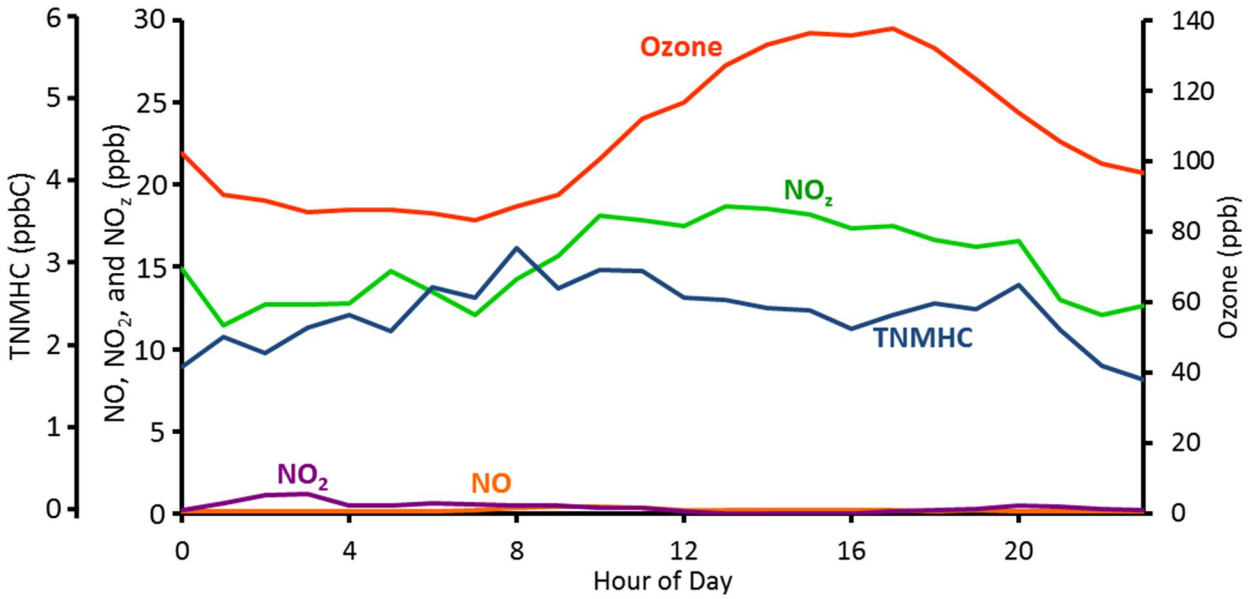

Figure 3-28. Diurnal average concentrations of ozone and precursors at Horsepool, 1-3 March.

Ozone production efficiency is the ratio of production of ozone and NO_2 (also called "odd oxygen" or O_x) to the removal of NO_x; more simply, it is the number of ozone molecules produced for each molecule of precursor consumed (Lin et al., 1988; Sillman, 1999). The linear regression slope of the relationship between ozone and NO_z (NO_z is the sum of NO_x reaction products, or $NO_y - NO_x$) and between O_x and NO_z have often been used to approximate ozone production efficiency, since the compounds that comprise NO_z are end products of NO_x photochemistry (e.g., Trainer et al., 1995). A higher ozone to NO_z slope indicates that more ozone is produced per molecule of NO_x consumed. Deposition or other loss of NO_z from the atmosphere is not accounted for in this metric, however, and a higher slope could also mean that NO_z is being removed more efficiently.

Figure 3-29 shows the slope of the relationship between ozone and NO_z at Horsepool on days with maximum ozone greater than 90 ppb, calculated as described by Chou et al. (2009). This figure provides evidence that ozone production efficiency increases from early to late winter in the Uinta Basin, probably because temperature and available solar energy increases. Since some of the increase in the ozone to NO_z slope over time could be due to increased NO_z deposition, the values in Figure 3-29 should be used with caution. The trend of increasing efficiency in ozone production from early to late winter, however, is likely to be robust.

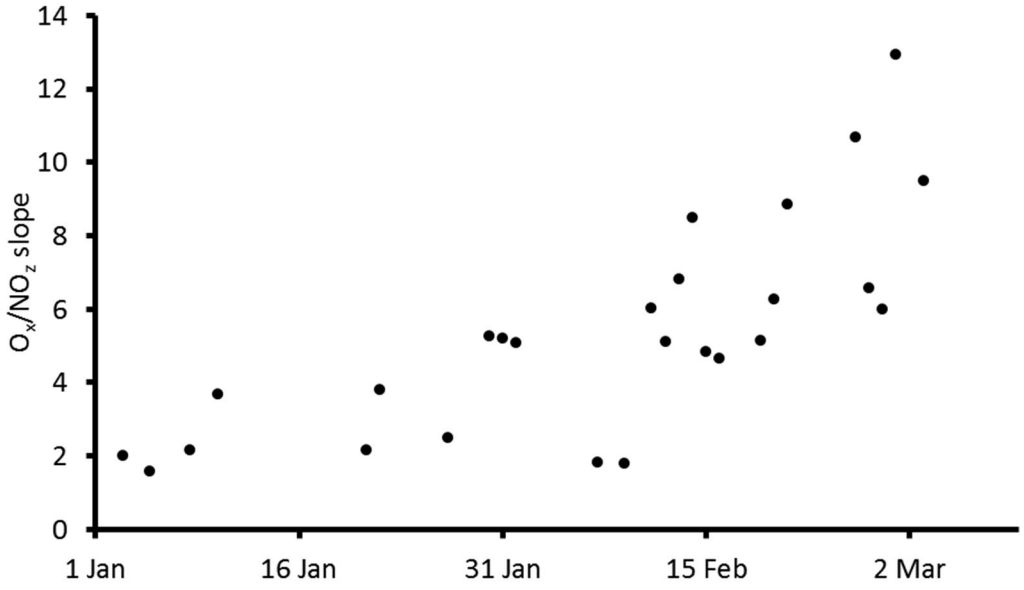

Figure 3-29. Slope of the linear regression relationship between O_x and NO_z at Horsepool, January-March. Only days with maximum ozone greater than 90 ppb are shown.

Photochemical indicators are metrics based on ambient measurements that can indicate whether ozone production in a region is more sensitive to VOC controls (VOC sensitive) or NO_x controls (NO_x sensitive) (Sillman, 1999). A number of photochemical indicators have been used, but the ratio of ozone to NO_y has been most commonly used and has been evaluated in a number of studies (Stein et al., 2005). The rationale for use of this indicator ratio, as explained by Sillman (1999), is that the major sinks for radicals in the ozone photochemical process are peroxides and NO_z, especially HNO_3. Radical production exceeds the rate of NO_x emissions in NO_x sensitive regimes, while the opposite is true in VOC sensitive regimes (see also Kleinman, 1994). In cases with more radicals than NO_x (NO_x sensitive), less NO_x is available to react with radicals to produce HNO_3 and other NO_z, so more peroxides are produced relative to HNO_3. In the opposite case, more HNO_3 and other NO_z can be expected. Thus, the ratio of peroxides to NO_z is a relative indicator of NO_x versus VOC sensitivity. Ozone production is proportional to the production of odd hydrogen radicals, and since direct peroxide measurements are rarely available, the ratio of ozone/NO_y or ozone/NO_z is often used.

Unfortunately, cutoff values or ranges that indicate NO_x versus VOC sensitivity in the ozone/NO_y ratio or other indicators can be different for different regions (Stein et al., 2005), and caution must be exercised in using cutoff values from other studies, especially when emissions or chemistry may be unique, as with wintertime ozone in the Uinta Basin. Determination of appropriate cutoff values to distinguish whether NO_x or VOC controls would be more effective is best achieved through utilization of a photochemical model, and indicator ratios can be useful for verifying model-based determinations of NO_x or VOC sensitivity.

Since a verified photochemical model is not yet available for the Uinta Basin, the value of the ratio of ozone/NO_y that would indicate NO_x versus VOC sensitivity cannot be reliably

determined. However, the transition between these two states is gradual, and higher ozone/NO_y ratios always indicate movement *towards* NO_x sensitivity (Sillman, 1999). Figure 3-30 shows that the ozone/NO_y ratio steadily increased from early to late winter in the Uinta Basin. The ozone/NO_z ratio, another common indicator, showed a similar trend (not shown). Together, these indicators provide evidence that more radicals are produced during late-season ozone events in the Uinta Basin (which also would tend to increase ozone production efficiency, as discussed above) and that early-season events are more likely to be VOC sensitive than late-season events.

In previous (urban summertime) studies, the transition region between NO_x and VOC sensitive regimes has been characterized by ozone/NO_y ratios between 5.6 and 15 (Stein et al., 2005). The ozone/NO_y ratio at Horsepool is within this range by mid-February, but it is inappropriate to use urban summertime studies in comparison with wintertime ozone production in the Uinta Basin. It is possible that VOC controls in the Uinta Basin will be more effective at reducing ozone than NO_x controls early in the year, but that NO_x controls will have increasing effectiveness as the winter season proceeds, but further work, including photochemical modeling, will be required to determine this definitively. Seasonal transitions from NO_x sensitivity in warm seasons to VOC sensitivity in cool seasons have been observed by others, and are likely due to decreased UV radiation and water vapor concentration, both factors that limit radical production (e.g., Jacob et al., 1995).

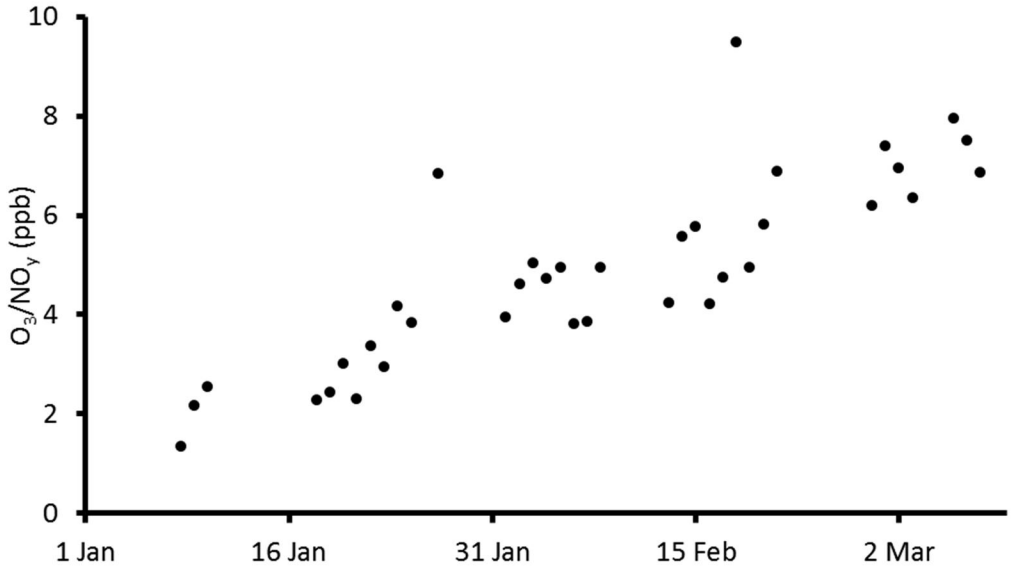

Figure 3-30. Ratio of ozone to NO_y at Horsepool, January-March. Only days with maximum ozone greater than 90 ppb are shown.

3.1.3.6 Interannual Variability in Wintertime Ozone

Figure 3-31 shows a time series of ozone concentrations at several sites in the Uinta Basin from July 2009 through 15 March, 2013. The Ouray and Red Wash air quality monitoring stations

began operation in July 2009. During winter 2009-10, both sites experienced multiple exceedances of the NAAQS for ozone (75 ppb). Subsequently, regulatory monitors in Roosevelt, Vernal, and Rangely were added. As Figure 3-31 shows, exceedances of the NAAQS have been observed during three of the four years in the Uinta Basin for which continuous ozone monitoring data is available. The Utah Department of Environmental Quality also measured ozone in Vernal during 2006 and 2007, but those data are not publicly available and are not included here. No wintertime exceedances of the NAAQS were measured during that period.

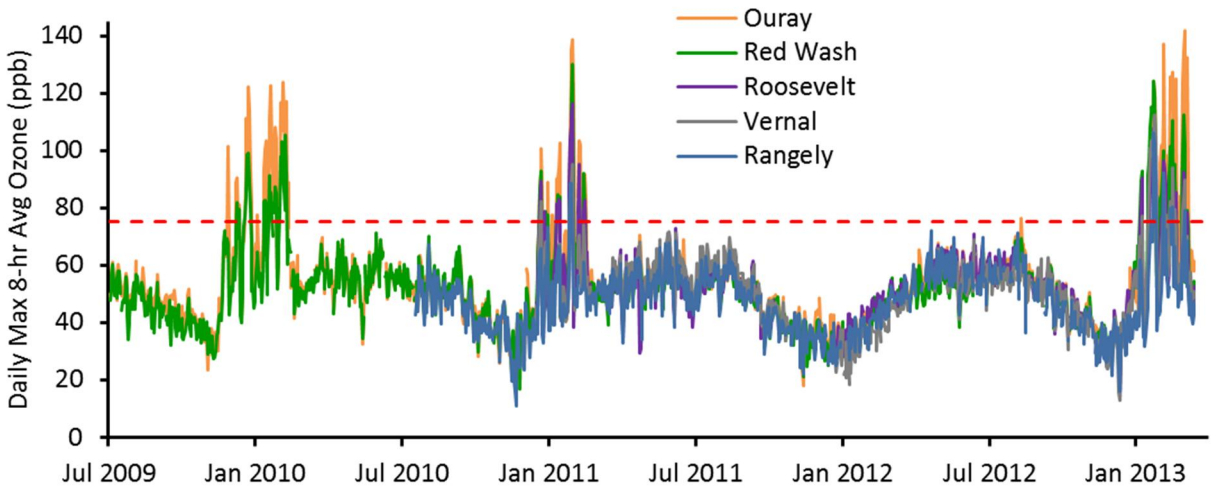

Figure 3-31. Time series of daily maximum 8-hour average ozone concentration at five sites in the Uinta Basin, July 2009-March 2013. The red dashed line shows 75 ppb, the EPA NAAQS for ozone.

Table 3-7 summarizes ozone statistics from the five sites shown in Figure 3-31 for each of the years that data are available. Data are organized by calendar year rather than by winter season, since summertime exceedances have also occurred (albeit rarely), and since a nonattainment designation, if made by EPA, will be based on the average of the annual fourth highest daily maximum 8-hour average concentration averaged over three consecutive calendar years (i.e., the "ozone design value"). Based on data collected between 1 January 2011 and 15 March 2013, the average of the three annual fourth highest daily maximum 8-hour average ozone concentrations at Rangely is 78 ppb and thus exceeds the 75 ppb ozone NAAQS. The Ouray and Red Wash sites are not regulatory, but their current ozone design values are 106.5 and 92.9 ppb, respectively. Ozone data has been collected in Vernal and Roosevelt since January 2011, but 2011 data were collected by USU and are not regulatory. These sites, as a result, only have two years of regulatory data. The two-year averages of the fourth highest regulatory value for Vernal and Roosevelt are 83.4 and 85.5, respectively. In order to maintain a design value less than 75 ppb, the fourth highest 8-hour average ozone concentration for 2014 will have to be no higher than 58 ppb for Vernal and 54 ppb for Roosevelt, which is unlikely.

Table 3-7. Ozone summary statistics for five sites in the Uinta Basin over five calendar years. The Vernal, Roosevelt, and Rangely sites are regulatory; Ouray and Red Wash are not. All values shown were calculated from daily maximum 8-hour average concentrations.

	Mean	Median	Max	Min	4th Highest Daily Max	# of Exceedance Days
2009						
Ouray	47.2	47.9	101.5	23.4	67.4	1
Red Wash	44.8	43.7	72.3	27.3	67.6	0
Vernal	--	--	--	--	--	--
Roosevelt	--	--	--	--	--	--
Rangely	--	--	--	--	--	--
2010						
Ouray	56.7	54.5	123.6	20.3	117.3	40
Red Wash	54.4	53.6	105.4	17.0	98.9	30
Vernal	--	--	--	--	--	--
Roosevelt	--	--	--	--	--	--
Rangely	42.3	42.2	67.2	11.1	58.8	0
2011 (Vernal and Roosevelt sites were operated by USU and were not regulatory)						
Ouray	54.0	52.8	138.6	18.1	119.6	24
Red Wash	51.6	51.8	130.2	21.3	98.3	21
Vernal	55.5	55.6	95.1	33.1	84.9	7
Roosevelt	56.2	54.7	116.3	29.3	103.6	19
Rangely	48.6	50.0	88.6	21.9	73.4	3
2012						
Ouray	49.3	50.5	76.5	18.8	67.6	1
Red Wash	47.5	48.8	69.5	21.5	66.4	0
Vernal	45.7	46.8	68.9	14.5	64.8	0
Roosevelt	50.3	51.6	70.9	14.6	67.0	0
Rangely	46.7	47.4	71.9	15.9	69.6	0
2013 (through 15 March)						
Ouray	81.8	79.8	141.6	38.4	132.4	39
Red Wash	74.8	73.6	124.0	38.8	114.0	36
Vernal	67.2	63.4	114.9	37.5	102.1	22
Roosevelt	68.0	64.2	110.8	37.0	104.0	29
Rangely	56.4	52.4	106.1	31.7	91.0	11

3.1.4 Summary

The spatial distribution of ozone and NMHC concentrations observed during winter 2012-13 largely can be explained by elevation and proximity to oil and gas production. This finding shows that ozone production in the Basin depends on intensity of inversions (elevation dependent) and intensity of emissions. The spatial distribution of ozone was found to be more closely correlated with NMHC than with NO_x, perhaps indicating that NMHC sources are more important than NO_x sources for ozone production, but 3D photochemical modeling will be required before a definitive determination can be made of the sensitivity of ozone production to NMHC versus NO_x.

Ozone production efficiency increased from early to late winter, allowing ozone to be produced more rapidly during later season ozone events, even while precursor concentrations were lower. During early winter, lower temperatures and reduced sunlight increase the likelihood that the Uinta Basin is VOC sensitive (i.e., VOC controls would be most effective at mitigating ozone pollution). It is possible that the Basin transitions from VOC to NO_x sensitivity as the winter proceeds.

Though ozone concentrations above 75 ppb have occurred during three of the past four winters in the Uinta Basin, only the Rangely monitoring station has the requisite three years of regulatory data to permit a nonattainment area designation. By 2014, the Vernal and Roosevelt stations are likely to meet this benchmark.

3.1.5 Acknowledgements

We are grateful to the Uintah Impact Mitigation Special Service District; the Utah Science, Technology, and Research Initiative; the Department of Energy; and Mr. Marc Bingham for financial support of this work. We thank the Bureau of Land Management for providing equipment for remote ozone monitoring and to Detlev Helmig and Chelsea Stevens of the University of Colorado for providing access to molybdenum converter-based NO_x data they collected at the Horsepool site. We are also grateful to the Utah Department of Environmental Quality for providing space for our monitors at Roosevelt.

3.2 Observations and Numerical Modeling of the Atmospheric Boundary Layer in the Uinta Basin

3.2.1 Introduction

The atmospheric boundary layer occurring during persistent cold air pools (PCAPs) can be highly variable in both space and time and is influenced by a wide range of atmospheric processes (Lareau et al., 2013). The Uinta Basin, being a deep and extensive basin with an ideal bowl-shaped topography, is sheltered during PCAPs from the effects of weak weather disturbances. However, moderate weather systems and the westerly winds associated with these disturbances typically impact the boundary-layer in the western third of the basin and the top portion of the cold pool throughout the remainder of the Uinta Basin as turbulent mixing occurs between the relatively calm, polluted surface-based cold air pool and the clean, windy, disturbed air aloft**.** The extensive horizontal scale and deep nature of the Uinta Basin results in intense, long-lived, and complex PCAPS. Below the inversion top capping the boundary-layer, multi-level stable layers with varying flow direction and intensity were often observed during the 2013 UBWOS.

A series of targeted meteorological measurements were conducted in the Uinta Basin in January and February 2013 with the specific goal to better characterize the boundary-layer (height, temperature, winds, cloud cover, multi-layered structures) in the Basin. The targeted observations consisted of two ceilometers to observe boundary-layer height and aerosol concentration; rawinsondes to observe the profiles of temperature, moisture, and wind from the boundary-layer and continuing high above the surrounding terrain; and a fixed and a mobile

weather station used in concert with the Mesowest network to characterize the surface meteorological conditions. The synthesis and ingestion of all available surface weather station data available from all UBWOS scientists into http://mesowest.utah.edu has also been conducted as a part of this study**.** A crucial contribution from this study to the larger UBWOS scientific data collection efforts is the inclusion of observations in the region from near the surface through the top of the inversion, which can extend in some cases up to 1000 m AGL in depth, and typically several hundred meters higher than tethersonde observations collected by other research teams.

In addition, numerical WRF modeling simulations are being conducted as part of this study to characterize basin-wide wind flow characteristics. Due to the complexity of the terrain around the basin, and the complex interactions between synoptic westerly flow and the underlying boundary-layer, scattered point measurements and profiles of winds in the basin have proven insufficient to characterize the basin winds as a whole. Analysis of wind profile measurements from rawinsondes at Roosevelt and the NOAA wind lidar at the Horsepool site illustrate the localized nature of boundary-layer flows. Consequently, we expect that measurements at either of these sites cannot be applied uniformly to the basin as a whole. Thus, a gridded hourly model forecast of winds in the boundary-layer in the Uinta Basin is being produced using the WRF model in addition to surface wind analyses from the Utah 2-Dimensional Variational Analysis (Tyndall and Horel, 2013) that incorporates Mesowest observations.

The study reported here adds crucial observations to the existing datasets available to characterize the meteorology of the boundary-layer and the region just above the boundary-layer in the Basin. This study shows (1) temporal variations in boundary-layer height, (2) multiple layering within the stable boundary-layer, (3) daytime easterly flows within the boundary-layer between the surface and 500 m aloft on some days, (4) significant impacts of westerly flow intrusions in the Basin, and (5) that low cloud cover is most frequently observed within the lowest portions of the basin.

3.2.2 Methods

3.2.2.1 Monitoring Sites and Observations

The location of the University of Utah meteorological monitoring sites as well as the location of all available Mesowest sites within the basin (http://mesowest.utah.edu ingests data from all available sources for surface meteorological data) are shown in Figure 3-32.

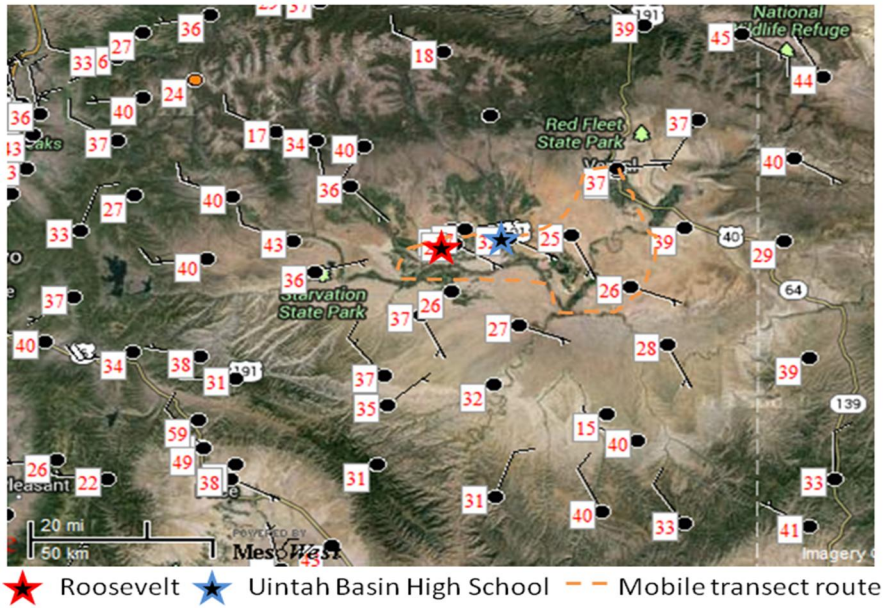

Figure 3-32. Location of key targeted University of Utah meteorological instrumentation sites and mobile transect route. All Mesowest stations available during the UBWOS are shown by black dots.

The meteorological monitoring for this study focused on the western part of the region identified as having high ozone levels (Lyman and Shorthill, 2013). This region was chosen to allow for spatial intercomparisons with meteorological observations conducted by other scientists at the Horse Pool and Ouray locations.

A CL-31 Viasala ceilometer was deployed between 17 January and 16 February 2013 at Roosevelt. A Viasala CK-12 Ceilometer was installed at the Uintah Basin High School in January and remained at that location through the entire 2012-13 UBWOS campaign. Graw DFM-06 radiosondes were launched at 1800 UTC from the Roosevelt site on the 26th of January, 16th of February, and every day between 1 February and 8 February, inclusive (except on 5 February when the radiosonde was launched from the Uintah Basin High School as part of an educational outreach activity). Photos of several of the key instruments are shown in Figure 3-33.

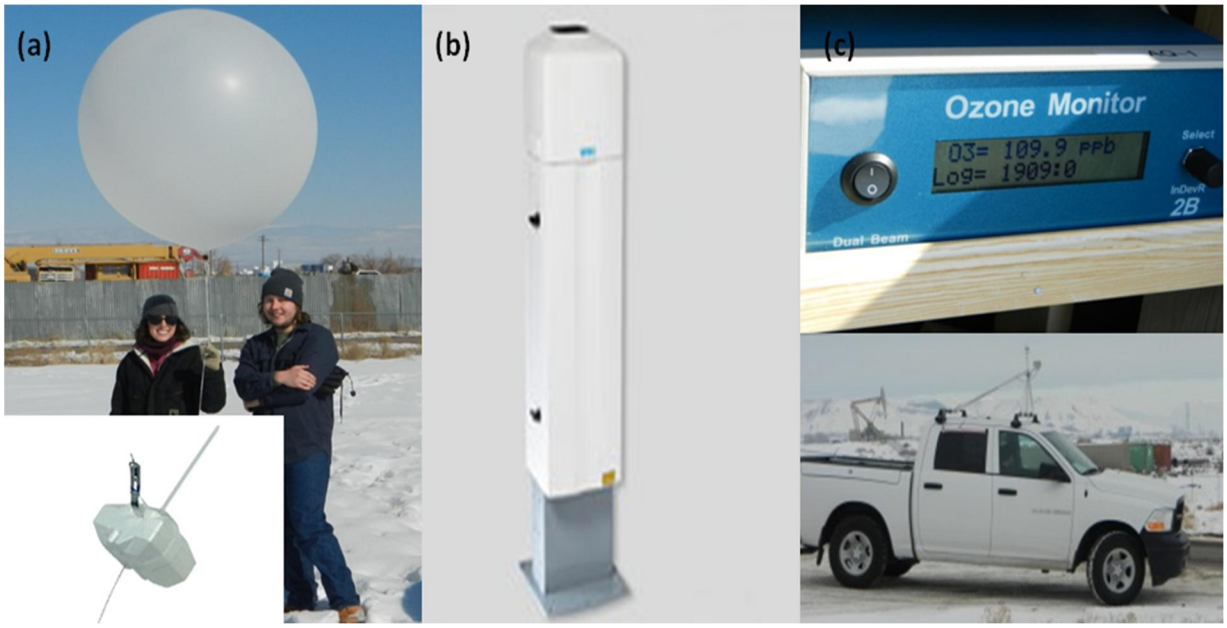

Figure 3-33. Instruments used during targeted meteorological observations in the Uinta Basin. (A) Graw DFM-06 radiosondes, (b), Viasala CL-31 ceilometer, (c) Meteorological and ozone mobile unit.

The coordinates (latitude, longitude, elevation) of the sites shown in Figure 3-32 as well as the instruments deployed at each site, the dates data were collected from these instruments, and the available processed data sets for general scientific use by the UBWOS scientists, as well as the temporal frequency of the data collected are listed in Table 3-8.

Table 3-8. University of Utah targeted meteorological observations location and dates.

Site Name	Latitude	Longitude	Elevation (m)	Instrument	Dates data collected (2013)	Available data	ΔT
Roosevelt	40.26560	-110.04120	1561	Viasala CL-31 ceilometer	19 January – 16 February	Excel file with hourly aerosol depth and median backscatter	1 hr
				Met station with sonic anemometer and net solar radiation	26 January – 16 February	Temperature, humidity, U, V, and W wind speed and direction, solar radiation	5 min

Site Name	Latitude	Longitude	Elevation (m)	Instrument	Dates data collected (2013)	Available data	ΔT
				GRAW DFM-06 rawinsonde	26 January; 1-4 January; 6-8 January; 16 February	Temperature, humidity, and wind speed and direction	1 second
Uintah River High School	40.282140	-109.86297	1544	Viasala CK-12 ceilometer	16 January – end of UBWOS	Excel file with aerosol depth	1 hr
				GRAW DFM-06 rawinsonde	5 January	Temperature, humidity, and wind speed and direction	1 sec
Mobile met and ozone	na	na	na	2B technologies 205;	25 January; 1, 2, 4, 6, 7, 16 February	Temperature, humidity, and wind speed and direction, ozone	1 min
Roosevelt	**40.26560**	**-110.04120**	**1561**	Viasala CL-31 ceilometer	19 January – 16 February	Excel file with hourly aerosol depth and median backscatter	1 hr
				Met station with sonic anemometer and net solar radiation	26 January – 16 February	Temperature, humidity, U, V, and W wind speed and direction, solar radiation	5 min
				GRAW DFM-06 rawinsonde	26 January; 1-4 January; 6-8 January; 16 February	Temperature, humidity, and wind speed and direction	1 second

The estimates of hourly aerosol depth from Roosevelt and the Uintah River High School has been used in combination with an algorithm searching for vertical gradients in ceilometers backscatter to calculate an estimate of boundary-layer depth each hour during cloud-free periods.

All targeted observations conducted during the UBWOS study by the University of Utah are available at http://home.chpc.utah.edu/~u0198116/ubos/obs.html, while all surface meteorological data from the Mesowest network in the Uinta Basin are archived at http://mesowest.utah.edu.

3.2.2.2 WRF Modeling

Numerical simulations of PCAP evolution in the Uinta Basin are being conducted. Hourly wind estimates for the basin surface and multiple levels aloft are currently being processed for the seven PCAPs that were observed during the UBWOS and will be available at the following website as the simulations are completed:
http://home.chpc.utah.edu/~u0198116/ubos/numerical.html.

Detailed information regarding the model set-up and domain used in the simulations are also available within those web pages.

3.2.3 Results and Discussion

3.2.3.1 Timing of Persistent Cold Air Pools During UBWOS

Seven persistent cold air pools were observed in the Uinta Basin between January and March 2013. The approximate starting and ending dates for these PCAPS are:

- PCAP 1: 6-11 January 2013 (~6 days)
- PCAP 2: 15-29 January 2013 (~15 days)
- PCAP 3: 31 January – 10 February 2013 (~11 days)
- PCAP 4: 12 – 17 February 2013 (~6 days)
- PCAP 5: 18-20 February 2013 (~3 days)
- PCAP 6: 26 February – 3 March 2013 (~6 days)
- PCAP 7: 6-9 March 2013 (~4 days)

During each of these PCAPs, variations in the boundary-layer height, intensity and depth of the vertical temperature inversion, and both boundary-layer winds and synoptic winds above the PCAP were observed. Hence, while it is difficult to generalize about Uinta Basin PCAPS, there were some characteristics observed during all PCAPS. First, the boundary-layer wind speeds were light and variable (less than 2 ms^{-1}) in the lowest portions of the valley such as Ouray and Horsepool, but were much stronger and variable along the mid-valley foothills into the higher foothills (5-15 ms^{-1}). Weak up valley flows during the day and down valley flows at night prevail within the major river valleys. The temperature inversions between the lowest elevations and the upper foothills varied in strength from isothermal conditions (temperature constant with height) to over 10 ^{o}C. The vertical distribution of the stability gradient varied widely during the UBWOS study, occurring several hundred meters above the surface during days with cloud-topped mixed layers to only a few 10s of meters above the surface on days with strong surface radiation inversions. In the following subsections we discuss in more depth the observational and numerical modeling findings regarding the boundary-layer characteristic in the Uinta Basin during the 2012-2013 UBWOS.

3.2.3.2 Boundary-Layer Height and Structure

The boundary-layer depth and structure during UBWOS persistent cold air pools were estimated using backscatter and backscatter gradients from the two University of Utah ceilometers deployed in the basin. On most days, distinct layering of the vertical structure of the boundary-layer backscatter was observed (Figure 3-34).

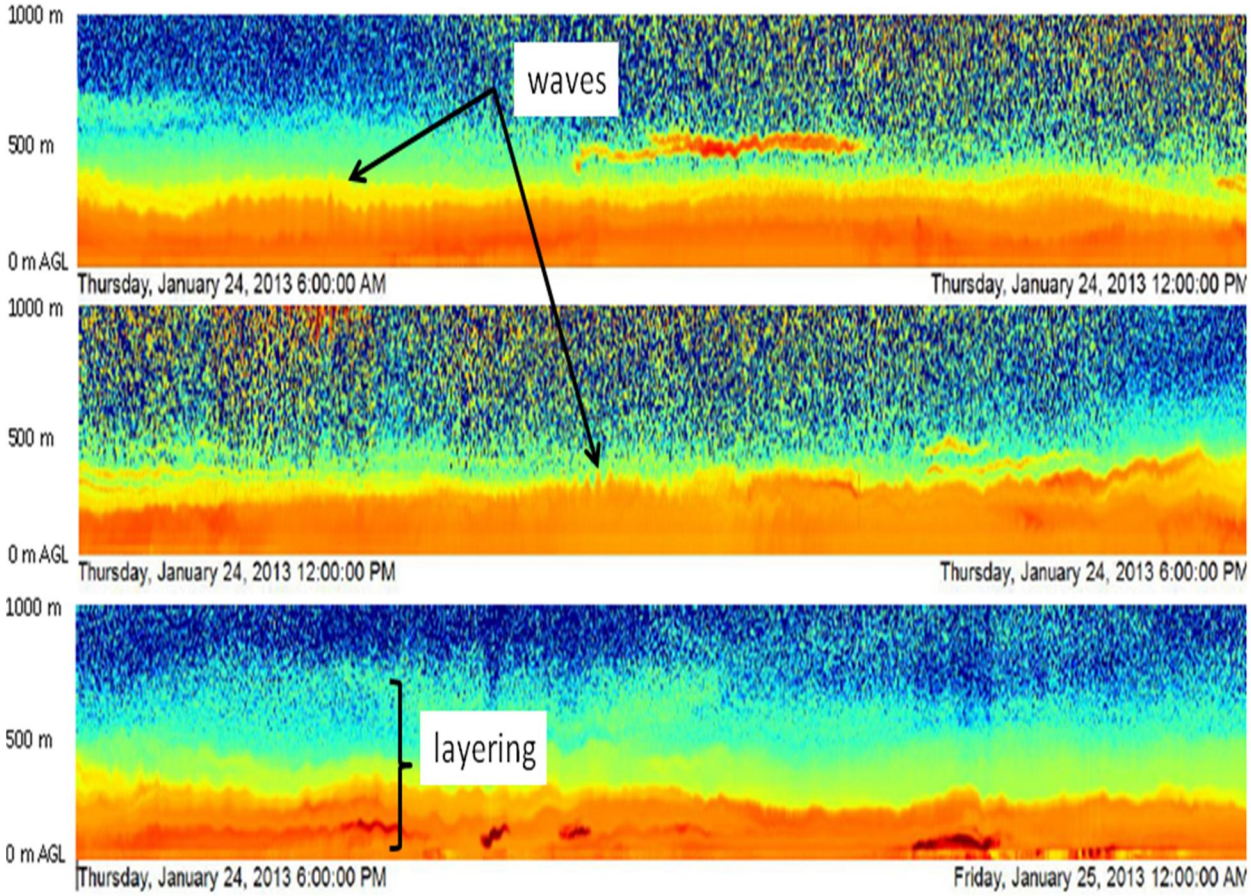

Figure 3-34. Ceilometer aerosol backscatter on 24 January 2013 at Roosevelt, UT. Higher backscatter denoted by warm colors and lower aerosol concentrations indicated by cool colors.

These layered structures in the vertical profile of aerosol backscatter were typically associated with layered structures in the vertical temperature and wind fields observed in the once-daily rawinsonde launches from Roosevelt (not shown, rawinsonde data available at U Utah UBWOS website). Along the top of the primary polluted boundary-layer, gravity waves were observed as seen in Figure 3-34. It is the depth of this primary surface layer that is used to estimate aerosol depth using gradient methods. Above the primary polluted layer located in the first 200-400 meters of the boundary-layer, a transition layer was sometimes observed. In this layer, mixing and dispersion from synoptic flows impinging on the top of the temperature inversion resulted in lower aerosol concentrations and the aforementioned gravity waves.

Alternating layers of high and reduced aerosol concentrations embedded within stable boundary layer were observed on numerous occasions. Another feature that is apparent from Figure 3-34 is the diurnal variations in the depth of the surface-based polluted layer. These diurnal variations are associated with similar variations in the temperature structure of the boundary-layer. On the 24th January (Figure 3-34), the depth of the surface-based polluted layer was observed to be near 300 m during the overnight hours, but increased to nearly 500 m during the afternoon. The depth of the aerosol layer observed during the UBWOS varied not only from day to day but also from one persistent cold air pool to another as shown in Figure 3-35.

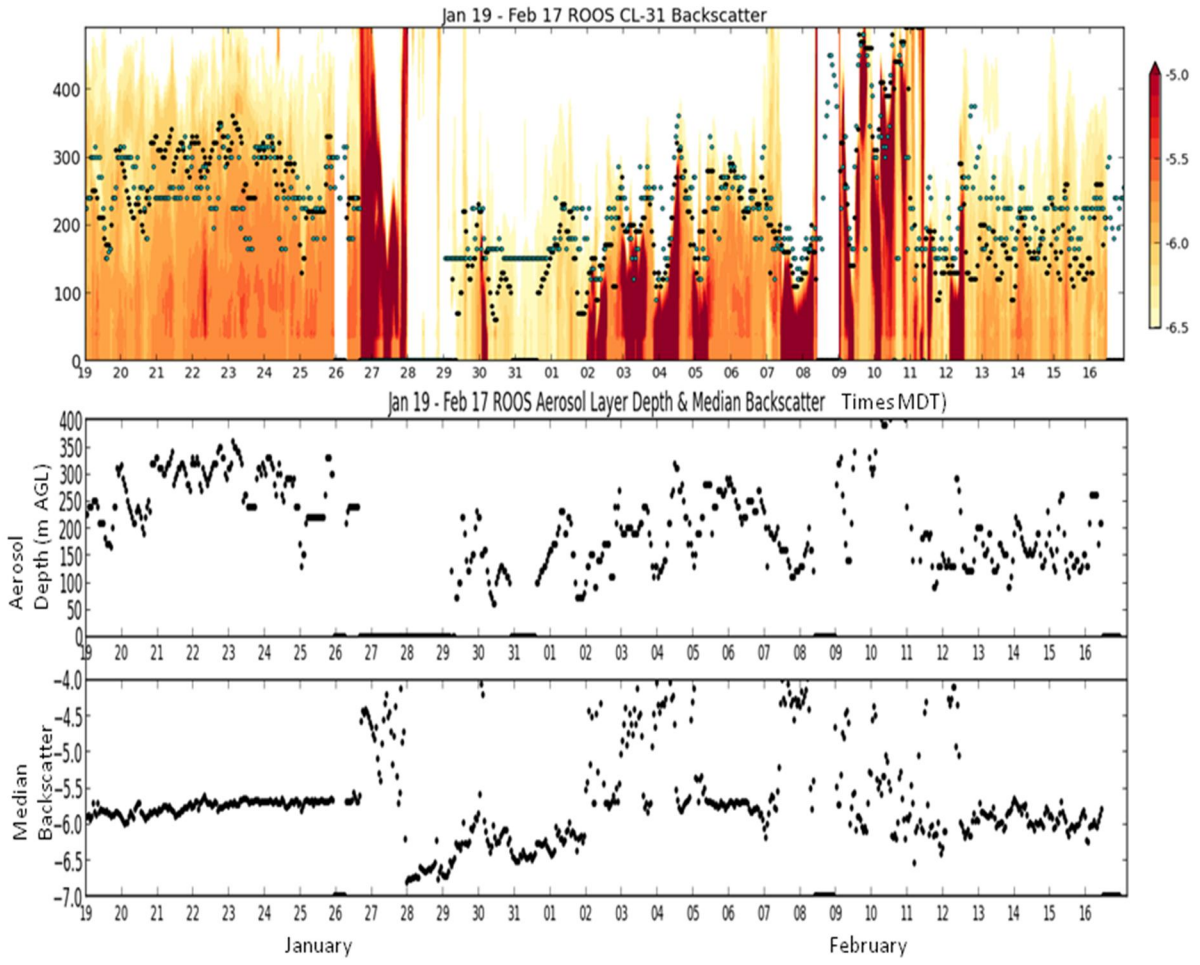

Figure 3-35. Aerosol backscatter between 19 January 2013 and 17 February 2013 at Roosevelt (top), depth of the dominant aerosol layer (middle) and median backscatter values for region below the calculated aerosol depth (bottom).

During PCAP 2, which occurred between 15-29 January 2013, the estimated depth of the primary aerosol later was 200-300 m AGL. During the following event (PCAP 3, 31 January – 10 February 2013), the primary aerosol layer showed significantly greater diurnal and temporal variation than during PCAP 2, with the mean aerosol depth approximately 100 m lower than

that observed during the preceding event. Fog, deeper cloud layers, and precipitation (dark red features in Figure 3-35) complicate the analysis of aerosol layer depth during PCAP 3. During PCAP 4 (12 – 17 February 2013), the mean aerosol depth was also approximately 100 m lower than that observed during PCAP 2.

3.2.3.3 Boundary-Layer Winds and Flow Interactions

Describing the boundary-layer winds in the Uinta Basin is challenging as a result of (1) limited wind data above the surface and (2) highly variable (both spatially and temporally) wind patterns evident in Mesowest surface observations, rawinsonde observations at Roosevelt, and lidar observations at Horsepool. Detailed meteorological analysis has resulted in identifying several noteworthy wind features in the Uinta Basin during UBWOS 2013:

Surface and rawinsonde observations indicate an easterly flow both at the surface and extending aloft through the western 2/3rd of the Basin (the extent and intensity of the easterly flow varies from day to day, modulated by the boundary-layer thermal structure and other unknown factors). However, insufficient data exists to quantify the importance of the elevated easterly flow in basin-wide transport at this time. Numerical modeling work is underway to address this issue. Figure 3-36 shows rawinsonde observations on two days during PCAP 3 on 2 and 4 of February 2013 when, within an elevated strong stable layer approximately 350 m deep, 2-4 ms^{1} easterly jets were observed. It is unclear whether the easterly flow is a return flow in response to the westerly flow forcing observed at the top of the inversion, and this question is an issue for future exploration.

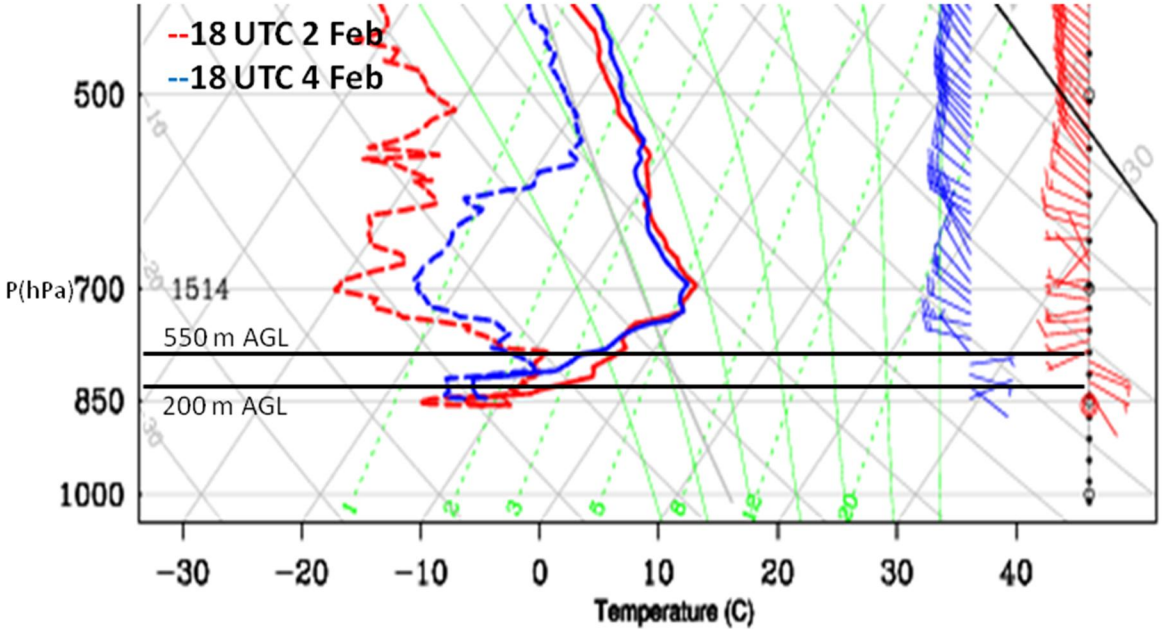

Figure 3-36. Skew-T plot showing temperature, dew point temperature, and wind speed and direction for 2 and 4 February 2013 at 1800 UTC.

Highly variable westerly wind intrusions were noted during most of the 7 PCAPs during the UBWOS. These winds resulted in turbulent mixing and dilution of the PCAP both at the top of the boundary layer and on the Western side of the basin. T hese winds resulted in dramatic fluctuations in temperature and pollutant concentrations in the Starvation Reservoir and Duchesne area and in some cases a strengthening of the temperature inversion as downslope flow warmed the air at the top of the PCAP. Modeling work is currently being conducted to address questions related to this issue. Figure 3-37 shows modeled variations in 775 mb winds speeds. Depending on elevation, the 775 mb level is 400-800 m above the ground surface and represents the winds at the top of the inversion during this episode.

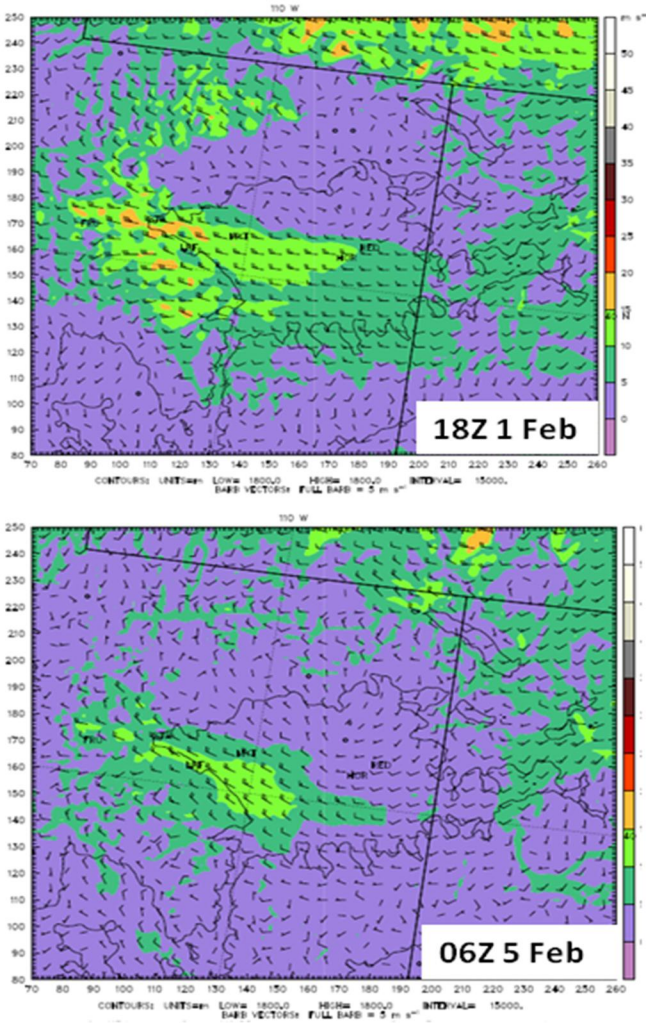

Figure 3-37. 775 hPa level wind speeds (shaded and barbs) and direction for WRF numerical simulations during the 30 January-10 February 2013 persistent cold air pool in the Uinta Basin.

It is important to recognize that these periods of strong westerly air bring in fresh, relatively unpolluted air into the Basin, and do not result in transport of ozone from the Wasatch Front into the Basin.

Additional numerical modeling of boundary-layer flows and interactions between synoptic and boundary-layer flows are being conducted at the University of Utah and the results of these modeling studies will be made available at the following website: http://home.chpc.utah.edu/~u0198116/ubos/numerical.html

3.2.3.4 Boundary-Layer Clouds

Boundary layer clouds were highly variable during the UBWOS study. The ceilometer data provides a quantitative measure of total cloudy hours during the UBWOS, as the ceilometers retrievals are quickly saturated by high backscatter from clouds. The spatial extent of clouds can be assessed from satellite imagery. Daily MODIS images from Aqua and Terra satellites can be accessed from the University of Utah UBWOS observations website. The extent of low cloud cover during the UBWOS PCAPS can be highly variable, as shown in Figure 3-38.

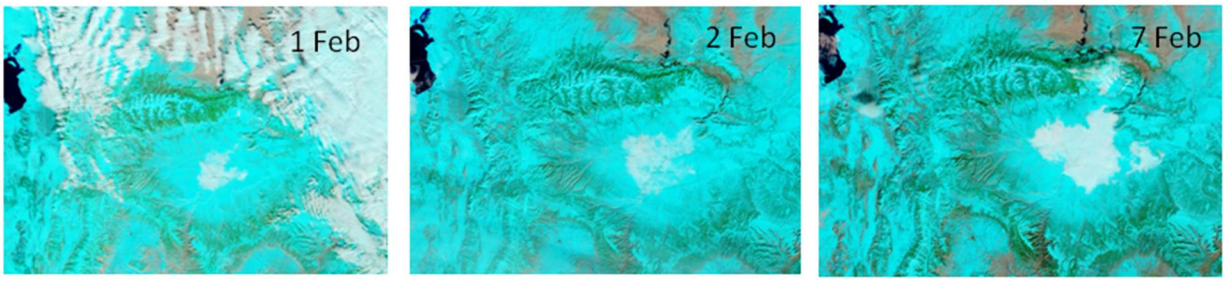

Figure 3-38. Afternoon MODIS satellite imagery showing snow (blue) and clouds (white) during 1, 2, and 7 February 2013.

For example, much of the basin was covered in clouds on 7 February, whereas only the region around Ouray was observing clouds during the afternoon satellite passes on 1 February. Estimates of low cloud occurrence and spatial extent in the basin during afternoons between 1 January – 12 March 2013 are listed in Table 3-9.

Table 3-9. Occurrence of low clouds in MODIS using AQUA satellite imagery data retrieved at mid-afternoon during UBWOS.

Date	Low cloud occurrence in Aqua satellite pass (Y, N or NAN (for obstructing high clouds)	Estimated fraction of basin (%) covered by low clouds
1 January	Y	<25%
2 January	N	
3 January	N	
4 January	N	
5 January	N	
6 January	N	
7 January	N	
8 January	N	
9 January	N	
10 January	N	
11 January	N	

Date	Low cloud occurrence in Aqua satellite pass (Y, N or NAN (for obstructing high clouds)	Estimated fraction of basin (%) covered by low clouds
12 January	N	
13 January	N	
14 January	N	
15 January	N	
16 January	N	
17 January	N	
18 January	N	
19 January	N	
20 January	N	
21 January	N	
22 January	N	
23 January	NAN-high clds	
24 January	NAN—high clds	
25 January	NAN—high clds	
26 January	NAN—high clds	
27 January	NAN—high clds	
28 January	NAN—high clds	
29 January	NAN—high clds	
30 January	N	
31 January	N	
1 February	Y	<10%
2 February	Y	<25%
3 February	N	
4 February	Y	<50%
5 February	N	
6 February	NAN-high clds	
7 February	Y	>50%
8 February	NAN-high clds	
9 February	Y	>50%
10 February	Y	>50%
11 February	Y	<50%
12 February	N	
13 February	N	
14 February	N	
15 February	N	
16 February	N	
17 February	N	
18 February	N	
19 February	N	
20 February	NAN-high clds	
21 February	N	
22 February	N	
23 February	NAN-high clds	
24 February	N	
25 February	N	
26 February	N	
27 February	N	

Date	Low cloud occurrence in Aqua satellite pass (Y, N or NAN (for obstructing high clouds)	Estimated fraction of basin (%) covered by low clouds
28 February	N	
1 March	N	
2 March	N	
3 March	N	
4 March	N	
5 March	N	
6 March	N	
7 March	N	
8 March	NAN-high clds	
9 March	N	
10 March	N	
11 March	N	
12 March	NAN-high clds	

3.2.4 Summary

Intense, long-lived PCAPs are common during winter and generally encompass the entirety of the Uinta Basin. Below the inversion top in the boundary-layer, complex multi-level stable layers with varying flow direction and intensity were often observed during the 2013 UBWOS.

Meteorological data from laser ceilometers, rawinsondes, and surface and satellite platforms during the UBWOS provide an enhanced view of the spatiotemporal evolution of the boundary-layer. The key data sets currently available for download at the University of Utah UBWOS study webpage are:

- Ceilometer estimates of Uinta Basin aerosol depth and relative intensity.
- Rawinsonde profiles of boundary-layer winds, temperature and moisture, as well as observations of the synoptic winds impinging on the PCAP from aloft.
- Transects of co-located meteorological data (temperature, humidity, winds) and ozone data in a circular loop from Roosevelt to Vernal, Horsepool, Ouray, Myton, and back to Roosevelt.
- Integration within MesoWest data archive of surface weather station data from all available networks (e.g., NWS, Utah State University, University of Utah, AIRNOW, Utah Dept Air Quality, SNOTEL).
- Numerical model simulations of basin-wind boundary-layer and synoptic winds.

In addition to providing this crucial information for retrospective model validation studies and volume budget calculations within the basin, this study showed that:

- Multi-layer structures often exist in both rawinsonde temperature and ceilometers backscatter profiles, indicating a complex multi-layer pattern of pollutant transport existing within the Basin.

- The depth of the boundary layer as measured by the laser ceilometer during UBWOS persistent cold air pools ranged from 70-400 m.
- Westerly intrusions of synoptic winds into the western portions of the Basin are relatively common occurrences and may affect transport patterns of pollutants in the boundary-layer (including driving return easterly flows). Numerical modeling experiments are currently being conducted to test this hypothesis.
- Easterly flows in the boundary-layer during the daytime were a commonly observed flow regime in the western 2//3rd of the basin. Numerical modeling will be conducted to determine if these flows are thermally-driven or dynamically-driven and whether they occur only during the afternoon or during nighttime as well.

3.3 Use of the CALMET Diagnostic Model to Simulate Winter Inversions

3.3.1 Introduction

The major precursors to ozone formation—NO_x and VOC—are emitted by a variety of sources. To determine the contributions to ozone production of these different sources in the Uinta Basin, meteorological models that accurately reproduce transport conditions during winter inversions are needed. A realistic meteorological model of the region will enable us to observe how pollutant transport from sources within and outside of the Basin affects ozone and precursor concentrations in the Basin.

Forecasting models such as the Weather Research and Forecasting (WRF) model, however, have difficulty accurately simulating winter inversion conditions. The CALMET diagnostic model, on the other hand, builds meteorological simulations from actual measurements of meteorological conditions, potentially allowing it to capture key features of winter inversions that are not accurately simulated by the physics parameterizations within WRF. Thus, in this work we sought to determine the value of CALMET as a diagnostic tool for meteorological conditions in the Basin. If successful, CALMET model output can be used to better understand transport patterns and inversion characteristics during ozone episodes.

3.3.2 Methods

We incorporated data from all available meteorological stations, both at the surface and aloft, from an intensive UBOS study period (28 January to 8 February) for input to the most current version (6.42) of CALMET, an EPA-approved modeling program. This program was recently employed in a similar study of ozone precursor transport in the Upper Green River Basin of southwestern Wyoming (Rairigh, 2010).

We utilized a horizontal grid resolution of 1.5 km^2, and a 300 × 300 km modeling domain that extends 9 to 75 km beyond each edge of the Uinta Basin. Meteorological data were extracted from stations located either inside or up to 80 km beyond this area in all directions. Table 3-10 lists the 68 stations used. A 3D rendering of the modeling domain is shown in Figure 3-39. Upper air data were extracted from sites at Salt Lake City, UT; Grand Junction, CO; Denver, CO; and Riverton, WY. Vertical layers used for the model are shown in Table 3-11, and range from 10 to 3,500 meters above ground level.

Table 3-10. Stations from which data were used in the CALMET model.

Station	Station Name	Station	Station Name
1	OURAY	35	ROOSEVELT
2	MEEKER AIRPORT	36	CHEPITA
3	VERNAL AIRPORT	37	FRUITLAND
4	HEBER AIRPORT	38	PRICE
5	BRYSON CANYON	39	PORTABLE RWIS
6	BADGER WASH	40	DRY RIDGE
7	CART CREEK	41	ROOSEVELT
8	HANNA NEAR DUCHESNE NW 24	42	LITTLE RED FOX
9	BLACK TAIL	43	MOUNTAIN HOME
10	NUTTERS RANCH	44	MOON LAKE NEAR ALTONA
11	KINGS PONIT	45	INDIAN CANYON SUMMIT
12	HORSE RIDGE	46	US-40 @STARVATION
13	UPPER SAND WASH	47	YELLWOSTONE DRAINAGE
14	YAMPA PLATEAU	48	WEST FORK BLACK SMITH
15	DIAMOND RIM	49	VERNAL
16	FIVE MILE	50	SPLIT MOUNTAIN
17	BEAR RIVER	51	UPPER P.R. CANYON
18	DRAGON ROAD	52	CURRANT CREEK PEAK
19	GREEN RIVER	53	†RANGELEY COLORADO
20	LADORE	54	NORWAY
21	HUNTER CREEK	55	DEER VALLEY
22	RATTLESNAKE BENCH	56	WILD HORSE
23	DINOSAUR NM SUCCESS	57	RIFLE
24	CRAIG MOFATT AIRPORT	58	WINTER RIDGE
25	BRUIN POINT	59	MYTON
26	HELPER @ US 6	60	RAYS VALLEY
27	CALICO	61	*SAND WASH
28	SOLDIER SUMMIT	62	*PARIETTE DRAW
29	PRICE AIRPORT	63	*SEVEN SISTERS
30	FLATTOP MOUNTAIN	64	*SEEP RIDGE
31	PINTO	65	*WELLS DRAW
32	HEBER US-40	66	*MOUNTAIN HOME
33	SALT LAKE CITY	67	*GUSHER
34	PRICE	68	*HORSEPOOL

*USU Sites †Site omitted because reported data were incomplete

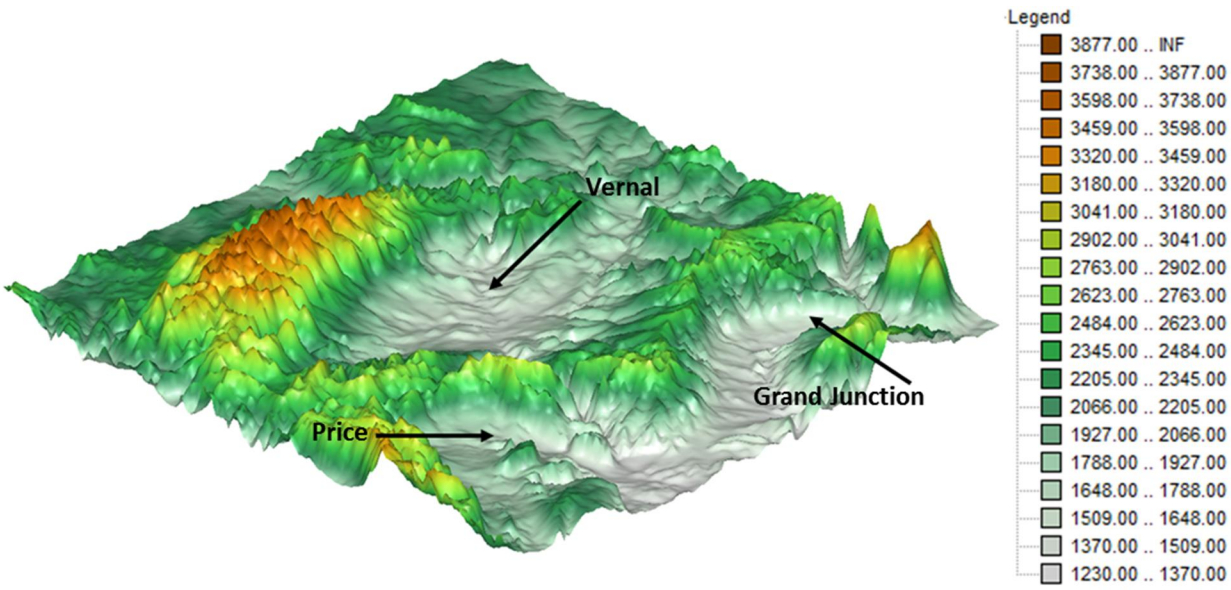

Figure 3-39. 3D elevation map of the CALMET modeling domain. Approximate locations of Vernal, Price, and Grand Junction are shown.

Table 3-11. Vertical layers utilized in the CALMET model.

Layer #	Layer top (m above ground level)
1	10
2	20
3	60
4	100
5	150
6	200
7	350
8	500
9	750
10	1000
11	2000
12	3000
13	3500

3.3.3 Results and Discussion

3.3.3.1 CALPUFF Model Animations

CALMET can be coupled with the 3D-modeling software CALPUFF, which generates animated plume dispersion models. In concert with this work, we created a video of a twelve-hour plume dispersion model that uses five hypothetical source points. These are publicly available online and illustrate the value of the CALMET modeling system (https://www.youtube.com/watch?v=5lTZeAfBSR4&feature=c4-overview&list=UUpUkAZfpeUBMmA_zAAERyZw).

3.3.3.2 Wind Speed and Direction

Ground-level (10 m) wind field vectors are shown below in Figures 3-40 through 3-43. Each of these figures was taken from 6 February 2013, the day of highest ozone concentration during an inversion period. On this day, the CALMET-predicted wind speeds within the Uinta Basin remained low (less than 3 m/s). At 3:00 local time (Figure 3-40), wind within the Basin flowed primarily from the south. By 9:00 (Figure 3-41), wind in the Basin was low and variable, but tended to blow mostly from east to west. This pattern held, for the most part, at 15:00 (Figure 3-42), but by 21:00 (Figure 3-43), winds were from the south on the east side of the Basin, and from the west on the west side of the Basin.

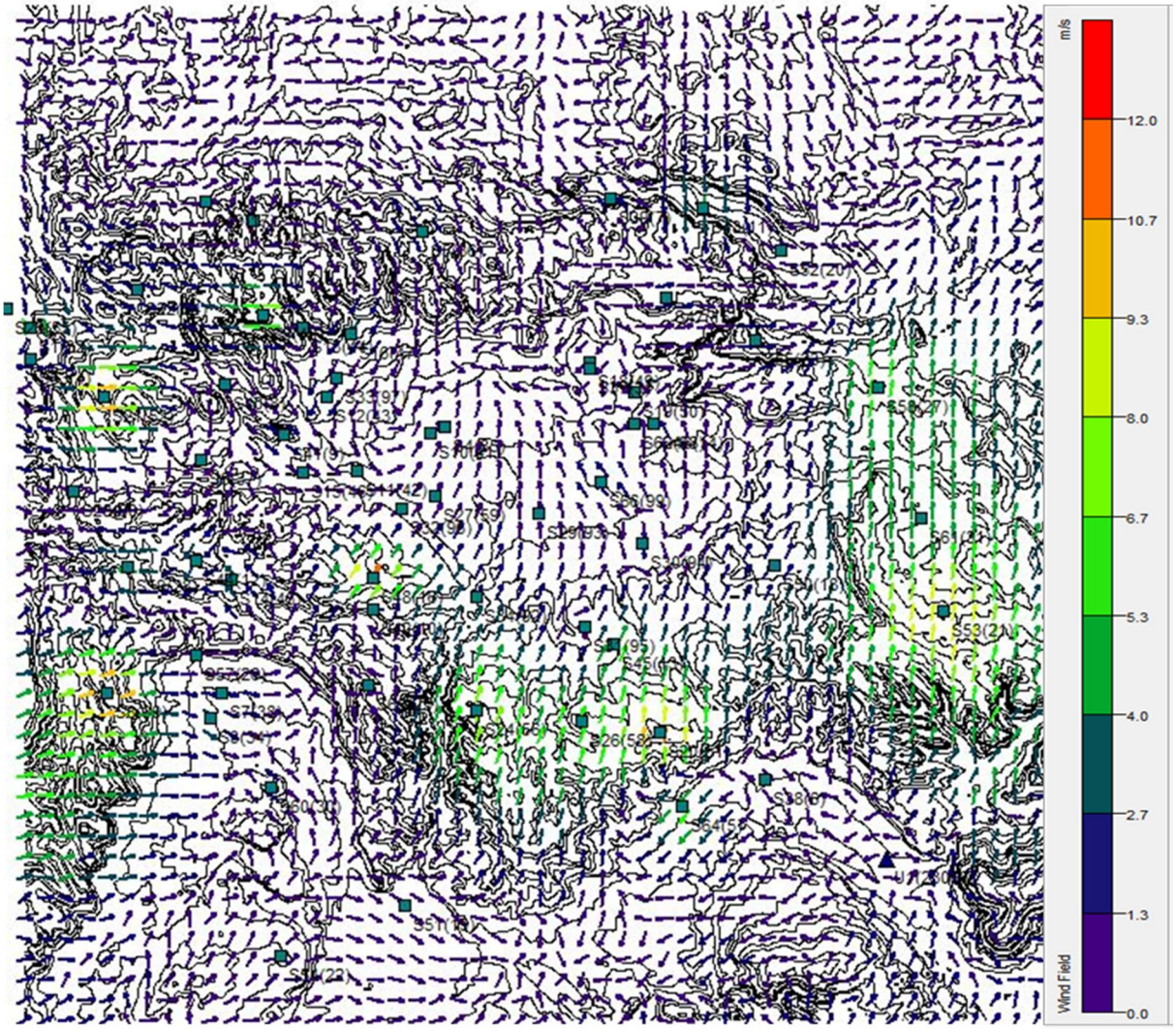

Figure 3-40. Ground-level (10 m) wind vectors at 3:00, 6 February.

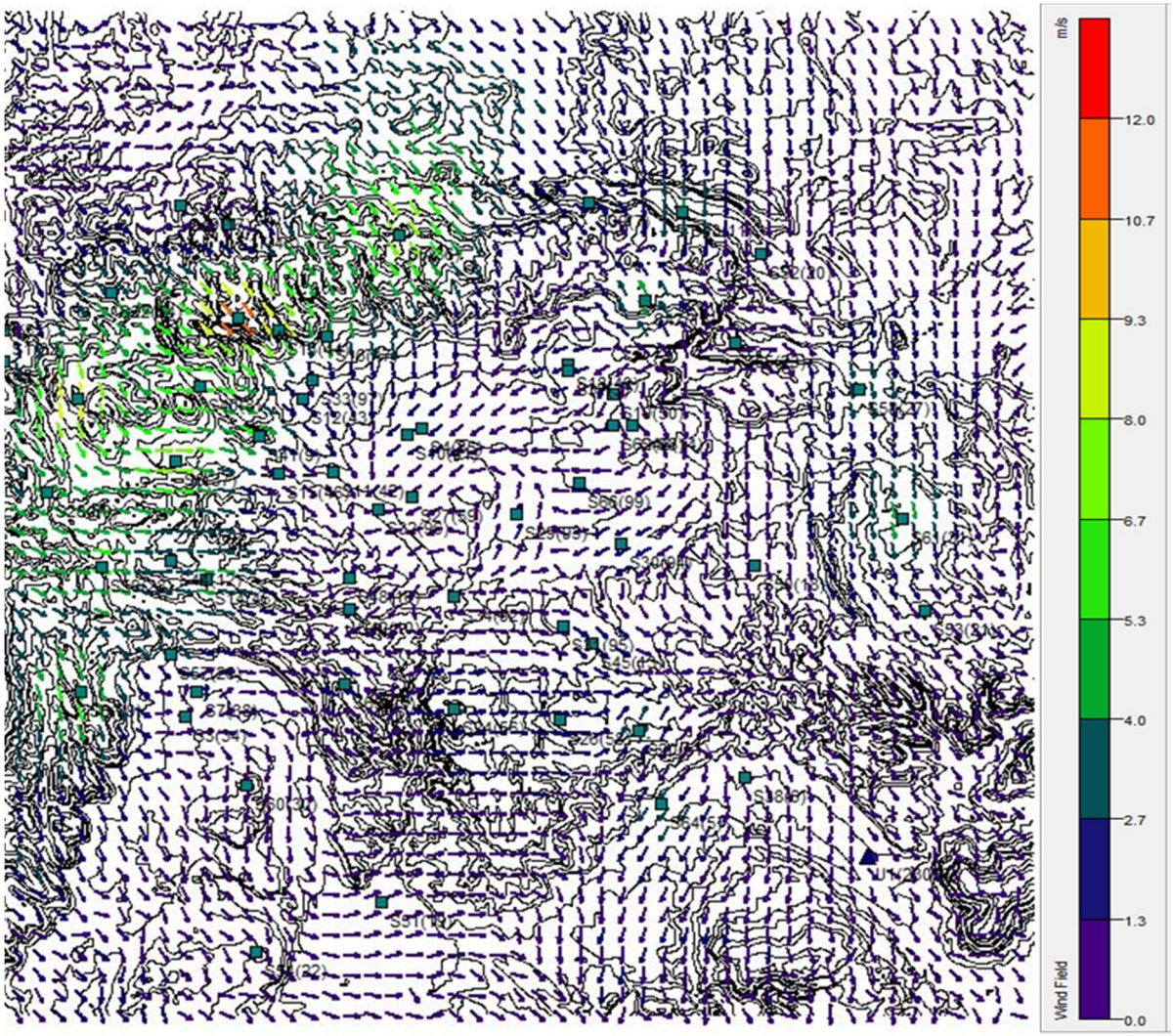

Figure 3-41. Ground-level (10 m) wind vectors at 9:00, 6 February.

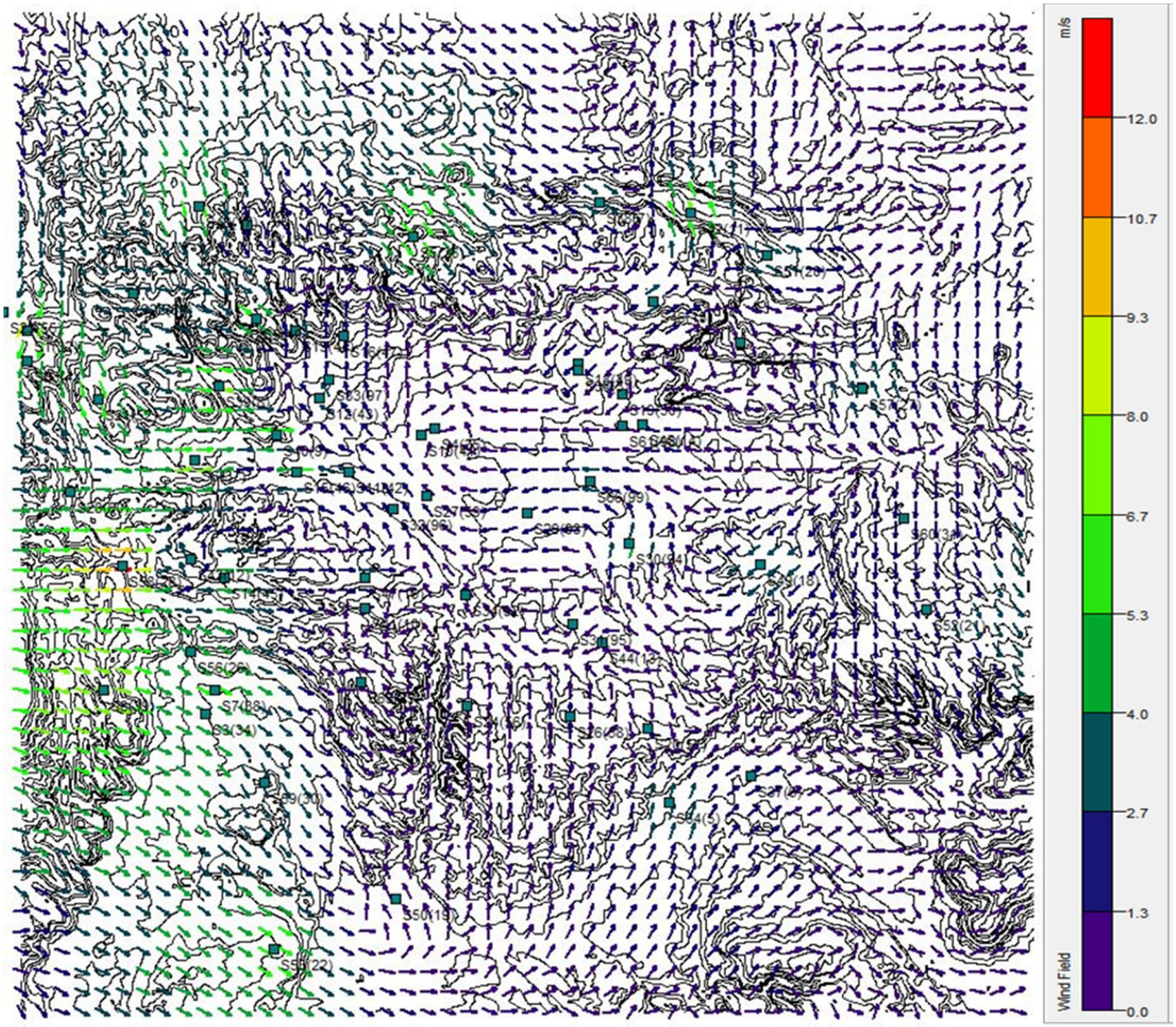

Figure 3-42. Ground-level (10 m) wind vectors at 15:00, 6 February.

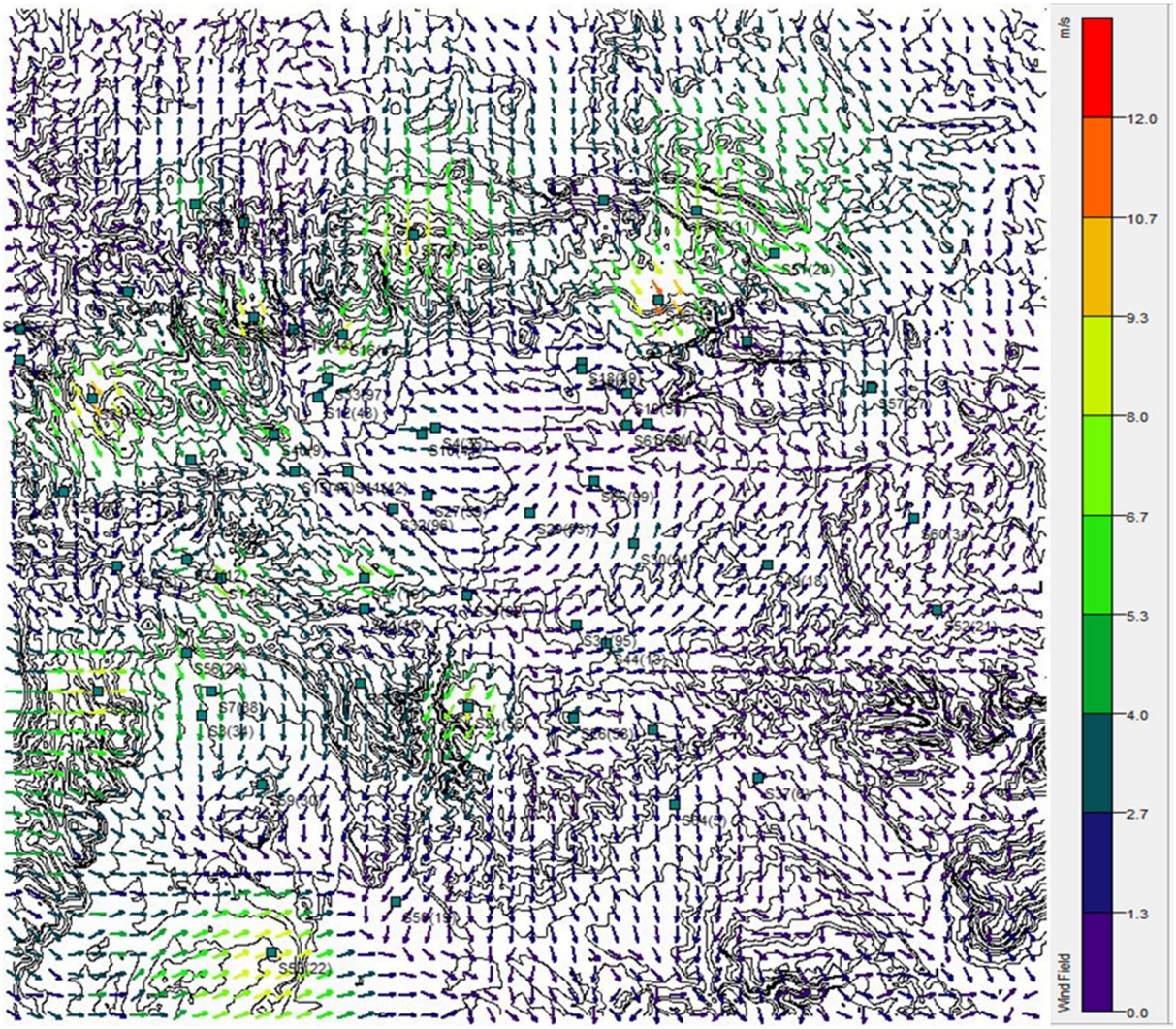

Figure 3-43. Ground-level (10 m) wind vectors at 21:00, 6 February.

We extracted ground-level (10 m) wind directions and speeds, as well as temperature, from the model at the locations of select surface meteorological stations and compared them with measured data. Table 3-12 shows results from two stations, Dragon Road and Sand Wash. Modeled and measured wind speed, wind direction, and temperature were well correlated at Dragon Road, but modeled and measured wind speed and direction were poorly correlated at Sand Wash. The Sand Wash site is located within Desolation Canyon, and at the 1.5 km horizontal resolution used, CALMET was not able to fully resolve terrain or wind patterns within the canyon. Also, measured wind speed was low, often zero, in Sand Wash, while modeled wind speed was never zero, further confounding the comparison.

Table 3-12. Slope, R^2 value, and percent deviation for the relationship between measured and modeled wind speed, wind direction, and temperature at the Dragon Road and Sand Wash sites. Percent deviation rows show values ± 95% confidence intervals.

	Dragon Road	Sand Wash
Wind Speed		
Slope	1.01	-0.03
R^2	1.00	0.01
Percent Deviation	0.8 ± 0.3%	20 ± 84%
Wind Direction		
Slope	0.68	0.19
R^2	0.59	0.02
Percent Deviation	7.8 ± 10.2%	9.4 ± 16.8%
Temperature		
Slope	0.93	1.04
R^2	0.85	0.92
Percent Deviation	0.0 ± 0.1%	0.3 ± 0.1%

3.3.3.3 Temperature

A surface-level temperature contour map for observations made at 10:00 local time on 7 February 2013 is shown in Figure 3-44. This figure shows an inversion, with areas of lowest elevation having temperatures less than 0 °C, and areas of highest elevation having temperatures up to about 10 °C. Site S49 shown in the upper left corner has a temperature of more than 20 °C, which is extremely unlikely for early February. We expect the temperature at this site is inaccurate, and it will be removed from future analyses.

To determine whether changes in temperature with height were being accurately simulated by the model, we extracted temperature from the different vertical layers of CALMET and compared them to temperature measured with a moored balloon on 6 February at Pariette Draw. Figure 3-45 shows the average measured and modeled vertical temperature profile for the period from 12:00 to 15:00. CALMET does simulate the presence of a temperature inversion, but the inversion occurs higher in the model than in reality, and the model predicts a decrease in temperature with height under the inversion that does not exist in the measurements, leading to a divergence of about 6 °C between measurements and the model at 275 m above ground.

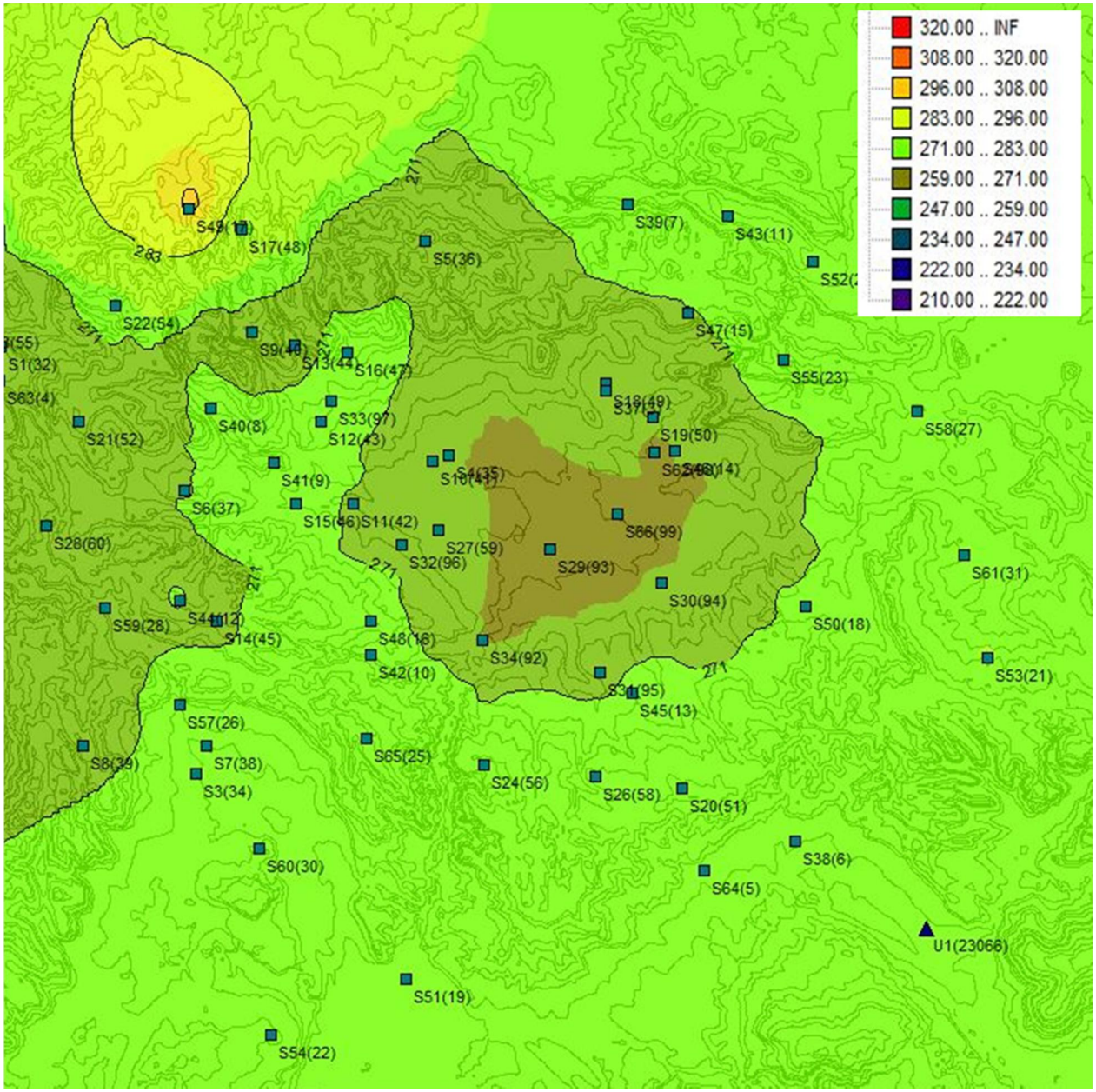

Figure 3-44. Surface temperature contour map for 10:00, 7 February.

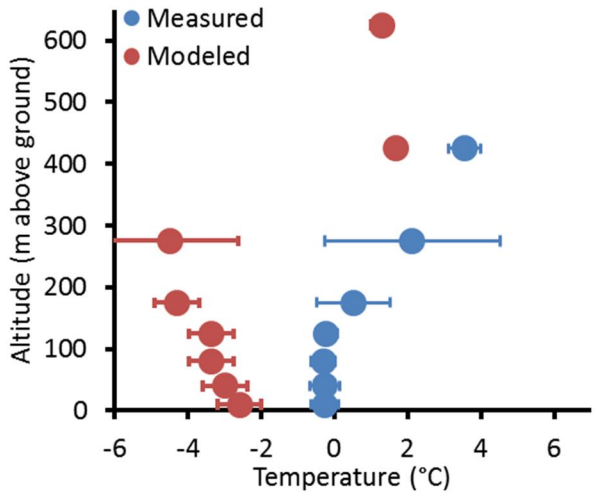

Figure 3-45. Measured and modeled vertical temperature profile for 12:00 to 15:00, 6 February at Pariette Draw.

3.3.4 Acknowledgements

We gratefully acknowledge funding for this project from the Uintah Impact Mitigation Special Service District.

3.4 References

Carter, W.P.L., 2009. *Development of the SAPRC-07 Chemical Mechanism and Updated Ozone Reactivity Scales*, College of Engineering, University of California, Riverside, California.

Chou, C.C., C.Y. Tsai, C.J. Shiu, S.C. Liu, and T. Zhu, 2009. Measurement of NO_y during campaign of air quality research in Beijing 2006 (CAREBeijing-2006): Implications for the ozone production efficiency of NO_x, *J. Geophys. Res., 114*, D00G01, doi: 10.1029/2008JD010446.

Doskey, P.V., J.A. Porter, and P.A. Scheff, 1992. Source fingerprints for volatile non-methane hydrocarbons, *J. Air Waste Manage. Assoc., 42*, 1437-1445.

EPA, 2003. *Interim Guidance on Control of Volatile Organic Compounds in Ozone State Implementation Plans, OAR-2003-0032*, Environmental Protection Agency, Research Triangle Park, North Carolina.

Hall, C., R. Anderson, M. Mansfield, S. Lyman, and H. Shorthill, 2013. *A Survey of Basins and Valleys in the Western U.S.A. for the Capacity to Produce Winter Ozone*, Office of Commercialization and Regional Development, Utah State University, Logan, Utah. Available at http://rd.usu.edu/files/uploads/2013_final_report_basins.pdf.

Jacob, D.J., L.W. Horowitz, J.W. Munger, B.G. Heikes, R.R. Dickerson, R.S. Artz, W.C. Keene, 1995. Seasonal transition from NO_x- to hydrocarbon-limited conditions for ozone production over the eastern United States in September, *J. Geophys. Res., 100*, 9315-9324.

Kleinman, L.I., 1994. Low and high-NO_x tropospheric photochemistry, *J. Geophys. Res., 99*, 16831-16838.

Lin, X, M. Trainer, and S.C. Liu, 1988. On the nonlinearity of tropospheric ozone, *J. Geophys. Res., 93*, 15879-15888.

Lyman, S. and H. Shorthill (Eds.), 2013. *Final Report: 2012 Uintah Basin Winter Ozone and Air Quality Study*, *CRD13-320.32*, Office of Commercialization and Regional Development, Utah State University, Logan, Utah.

Lyman, S.N, and M.S. Gustin, 2009. Determinants of atmospheric mercury concentrations in Reno, Nevada, U.S.A., *Sci. Tot. Environ., 408*, 431-438.

Martin, R.S., K. Moore, M. Mansfield, S. Hill, K. Harper, and H. Shorthill, 2011. *Final Report: Uinta Basin Winter Ozone and Air Quality Study, EDL/11-039*, Energy Dynamics Laboratory, Utah State University Research Foundation, Logan, Utah.

MSI, 2013. *Final Report: 2013 Upper Green Winter Ozone Study,* Meteorological Solutions, Inc. and T&B Systems, August. (Available at http://deq.state.wy.us/aqd/Upper%20Green%20Winter%20Ozone%20Study.asp).

Rairigh, K., 2010. *Draft Upper Green River Winter Ozone Study: CALMET Database Development – Phase II,* Wyoming Department of Environmental Quality, Cheyenne, Wyoming.

Sillman, S., 1999. The relation between ozone, NO_x, and hydrocarbons in urban and polluted rural environments, *Atmos. Environ., 33*, 1821-1845.

Stein, A.F., E. Mantilla, M.M. Millan, 2005. Using measured and modeled indicators to assess ozone-NO_x-VOC sensitivity in a western Mediterranean coastal environment, *Atmos. Environ., 39*, 7167-7180.

Trainer, M., B.A. Ridley, M.P. Buhr, G. Kok, J. Walega, G. Hubler, and D.D. Parrish, 1995. Regional ozone and urban plumes in the southeastern United States: Birmingham, a case study, *J. Geophys. Res., 100*, 18823-18834.

Tyndall, D., and J. Horel, 2013. Impacts of mesonet observations on meteorological surface analyses, *Wea. Forecasting, 28,* 254-269.

Webb, D., 2011. 'Big-city' ozone goes rural, *The Daily Sentinel: Grand Junction, Colorado*, March 24.